

The HELLAS2XMM survey: VIII. Optical identifications of the extended sample. [★]

F. Cocchia^{1,2,3}, F. Fiore¹, C. Vignali^{4,5}, M. Mignoli⁵, M. Brusa⁶, A. Comastri⁵, C. Feruglio^{1,2}, A. Baldi⁷, N. Carangelo⁸, P. Ciliegi⁵, V. D’Elia¹, F. La Franca⁹, R. Maiolino¹⁰, G. Matt⁹, S. Molendi⁸, G.C. Perola⁹, S. Puccetti^{1,11}

¹ INAF-Osservatorio Astronomico di Roma

via Frascati 33, Monteporzio-Catone (RM), I-00040 Italy

² Dipartimento di Fisica, Università di Roma Tor Vergata

Via della Ricerca Scientifica 1, I-00133 Rome, Italy

³ INAF-Osservatorio Astronomico di Brera via Brera 28, I-20121 Milano, Italy. e-mail: cocchia@brera.mi.astro.it

⁴ Dipartimento di Astronomia, Università di Bologna

via Ranzani 1, I-40127 Bologna, Italy

⁵ INAF-Osservatorio Astronomico di Bologna

via Ranzani 1, I-40127 Bologna, Italy

⁶ Max Planck Institut für Extraterrestrische Physik (MPE)

Giessenbachstr. 1, D-85748 Garching, Germany

⁷ Harvard-Smithsonian Center for Astrophysics (CfA)

60 Garden str, Cambridge 02138 MA, USA

⁸ INAF-IASF

via Bassini 15, I-20133 Milano, Italy

⁹ Dipartimento di Fisica, Università Roma Tre

via della Vasca Navale 84, I-00146 Roma, Italy

¹⁰ INAF-Osservatorio Astrofisico di Arcetri

Largo Enrico Fermi 5, I-50125 Firenze, Italy

¹¹ ASI Science Data Center, ASDC c/o ESRIN

via G. Galilei, 00044 Frascati, Italy

October, 10 2006

ABSTRACT

Aims. Hard X-ray, large-area surveys are a fundamental complement of ultra-deep, pencil-beam surveys in obtaining a more complete coverage of the AGN luminosity–redshift plane and finding sizeable samples of “rare” AGN.

Methods. We present the results of the photometric and spectroscopic identification of 110 hard X-ray selected sources from 5 additional XMM–Newton fields, nearly doubling the original HELLAS2XMM sample. Their 2–10 keV fluxes cover the range $6 \times 10^{-15} - 4 \times 10^{-13}$ erg cm⁻² s⁻¹ and the total area surveyed is ~ 0.5 deg² at the bright flux limit. We spectroscopically identified 59 new sources, bringing the spectroscopic completeness of the full HELLAS2XMM sample to almost 70% over a total area of ~ 1.4 deg² at the bright flux limit. We found optical counterparts for 214 out of the 232 X-ray sources of the full sample down to $R \sim 25$. We measure the flux and luminosity of the [OIII] λ 5007 emission line for 59 such sources.

Results. Assuming that the most high X-ray-to-optical flux ratio sources are obscured QSOs, we use the full HELLAS2XMM sample and the CDF samples, to estimate their logN–logS. We find an obscured QSO surface densities of 50 ± 23 and $100\text{--}400$ deg⁻² down to flux limits of 10^{-14} and 10^{-15} erg cm⁻² s⁻¹, respectively. At these flux limits the fraction of X-ray selected obscured QSO turns out to be similar to that of unobscured QSO. Since X-ray selection misses most Compton thick AGN, the number of obscured QSO may well outnumber that of unobscured QSOs.

We find that hard X-ray selected AGNs with detected [OIII] emission span a wide range of $L_{2-10\text{keV}}/L_{[\text{OIII}]}$ with a logarithmic median of (2.14 ± 0.38) . This is marginally higher than that of a sample of optically selected AGNs (median 1.69 and interquartile range 0.30), suggesting that optically selected samples are at least partly incomplete, and/or [OIII] emission is not a perfect isotropic indicator of the nuclear power. The seven X-ray Bright, Optically Normal Galaxy (XBONG) candidates in the sample have $L_{2-10\text{keV}}/L_{[\text{OIII}]} \gtrsim 1000$, while their X-ray and optical luminosities and obscuring column density are similar to those of narrow-line AGNs in the same redshift interval (0.075–0.32). This suggests that while the central engine of narrow-line AGNs and XBONGs looks similar, the narrow-line region in XBONGs could be strongly inhibited or obscured.

1. Introduction

Deep *Chandra* and XMM-*Newton* hard X-ray surveys have been able to detect the sources making the majority of the Cosmic X-ray Background (XRB) below 6–7 keV (Giacconi et al. 2002, Bauer et al. 2004, Moretti et al. 2003, Worsley et al. 2004, Brandt & Hasinger 2005). However, deep surveys cover only a fraction of square degree of sky making difficult to find sizable samples of medium- and high-luminosity sources. To obtain a more complete coverage of the redshift-luminosity plane, complementing deep surveys, and to compute an accurate luminosity function over wide luminosity and redshift intervals, a much larger area, of the order of a few square degrees, needs to be covered. Furthermore, large-area surveys can also provide sizeable samples of “rare” objects. To these purposes, we are carrying out the HELLAS2XMM serendipitous survey using suitable XMM-*Newton* archival observations (Baldi et al. 2002). As a first step, we have presented in Fiore et al. (2003) the optical identification of 122 hard X-ray selected sources detected in five XMM-*Newton* fields (hereafter the 1dF sample). Here we report the results of the photometric and spectroscopic identification of 110 X-ray sources from five additional XMM-*Newton* fields, hereafter the HELLAS2XMM second source sample, nearly doubling the original HELLAS2XMM sample and bringing the total area surveyed to about 1.4 deg² at a flux limit of $\sim 10^{-13}$ erg cm⁻² s⁻¹.

One of the most interesting findings of the optical identifications of the HELLAS2XMM sample, as well as of other hard X-ray selected *Chandra* and XMM-*Newton* surveys (see, e.g., ChaMP: Silverman et al. 2005; SEXSI: Eckart et al. 2005; CLASXS, CDFN, CDFS: Barger et al. 2005; CDFS, CDFN: Giacconi et al. 2002, Hasinger et al. 2003; XMM/2dF Georgakakis et al. 2004; HBS: Della Ceca et al. 2004) is the discovery that AGN activity spans a range of properties much wider than it was thought based on optically and soft X-ray selected AGNs. Indeed, hard X-ray selection provides a more complete view of AGN activity, being more efficient in selecting sources possibly missed by selection in other bands. For example, obscured and low-luminosity AGN several of which are left out in optical or soft X-ray selected samples. While most of optically and soft X-ray selected AGNs have an X-ray-to-optical (R-band) flux ratio X/O¹ between 0.1 and 10 (see, e.g., Maccacaro et al. 1988, Laor et al. 1997, Hasinger et al. 1998, Mineo et al. 2000), XMM-*Newton* and *Chandra* hard X-ray surveys have selected AGNs with X-ray-to-optical flux ratio well outside this range. In particular, the HELLAS2XMM survey has detected both a population of relatively bright X-ray sources with faint optical counterparts (and thus characterized by high X/O values; Fiore et al. 2003) and several X-ray sources in otherwise inactive and optically bright galaxies (with relatively low X/O ratios; named X-ray bright, optically nor-

mal galaxies, XBONGs, Fiore et al. 2000, Comastri et al. 2002).

The former population includes about 15–20% of the sources selected in the 2–10 keV band to have X/O more than one order of magnitude higher than that of typical broad-line, type 1 AGNs. Based on optical spectroscopy (Fiore et al. 2003), optical-to-near-infrared colors (Mignoli et al. 2004), near-infrared (Maiolino et al. 2006) and X-ray spectroscopy (Perola et al. 2004), we concluded that the majority of the HELLAS2XMM sources with X/O $\gtrsim 10$ are optically obscured QSOs at $z \gtrsim 1$. At fainter X-ray and optical fluxes, the situation is less clear, mainly because most of the optical counterparts of the high X/O sources are inaccessible to optical spectroscopy even with 10m-class telescopes.

The XBONGs, on the other hand, are found at low redshift (~ 0.1 – 0.3), with X-ray luminosities between 10^{42} and 10^{43} erg s⁻¹, bright optical counterparts ($R < 21$), thus relatively low X/O, and absorption-dominated optical spectra without strong nuclear emission (Comastri et al. 2002). It has been suggested that XBONGs selected in *Chandra* and XMM-*Newton* surveys are actually typical AGNs classified as normal galaxies just because of some observational biases (dilution of the nuclear spectrum by the host galaxy, inadequate set-up for optical spectroscopy in terms of wavelength range covered, signal-to-noise ratio, spatial resolution, see e.g. Moran et al. 2002, Severgnini et al. 2003, Georgantopoulos & Georgakakis 2005).

In this paper we present the optical identification follow-up observations of five additional fields of the HELLAS2XMM survey and focus the discussion on both the high X/O sources and the XBONGs, providing quantitative constraints to the space density of highly optically obscured, high-luminosity QSOs and proposing a quantitative definition of XBONGs. The paper is organized as follows: Sections 2 and 3 present the results of the optical photometric and spectroscopic identifications of the HELLAS2XMM second source sample; Section 4 discusses our main findings; Section 5 reports our conclusions. A $H_0 = 70$ km s⁻¹ Mpc⁻¹, $\Omega_M = 0.3$, $\Omega_\Lambda = 0.7$ cosmology is adopted throughout.

2. Optical identifications

The HELLAS2XMM second source sample includes sources detected in the 2–10 keV band in five XMM-*Newton* fields: A1835, IRAS13349+2438, GD153, Mrk421, BPM16274 (see Baldi et al. 2002 for details on the observations and X-ray data reduction). We have obtained relatively deep (exposure time 3–15m per image, limiting magnitude $R=24$ – 25) optical images for the majority of the sources in these five fields using EFOSC2 at the ESO 3.6m telescope, FORS1 at VLT and DOLORES at the TNG.

We exclude from the following analysis those areas, in the five fields, not covered by R-band images. This, together with the fact that Mrk421 field has been observed in win-

¹ $X/O = \log \frac{f_X}{f_R} = \log f_X + \frac{R}{2.5} + C$, where C depends on the chosen X-ray band and optical filter.

dow mode and that a large-area centered on the A1835 cluster of galaxies has been excluded from the analysis, reduces the total area surveyed to about 0.5 deg^2 . The total number of hard X-ray selected sources making the HELLAS2XMM second source sample is 110, bringing the total number of sources in the full HELLAS2XMM sample with optical coverage to 232 in ten XMM-Newton fields.

Optical images were bias subtracted, flat-field divided, and flux calibrated using observations of standard stars acquired during each night. Optical and X-ray images were brought to a common astrometric reference frame using bright AGNs (from 5 to 15 AGNs per field). Typical systematic shifts were of the order of $1''$, the maximum shift was of $\sim 2''$.

Source detection in the optical images was performed using the SExtractor package (Bertin et al. 1996) and we visually searched for optical counterparts of the X-ray selected sources within a conservative matching radius of 6 arcsec from the astrometrically corrected X-ray centroid. For X-ray sources with multiple optical counterparts we provide, in Table 1, the probability P of chance coincidence² (see also Brusa et al. 2003).

Optical counterparts brighter than $R \sim 24.5$ within $\sim 6''$ from the X-ray position were found for 103 sources. For 15 of them there are two candidate counterparts inside the X-ray error-box. Table 1 gives for each source the X-ray position, the position of the most likely optical counterpart (identified on the basis of its magnitude, displacement from the X-ray position and probability of chance coincidence, classification of the optical spectrum), the displacement between the X-ray and optical positions, the X-ray flux and the R magnitude (or lower limit) of the optical counterpart. In three cases, more than one optical source might contribute to the detected X-ray emission (see notes to Table 1).

The average displacement between the X-ray centroid and the position of the most likely optical counterparts is of $2.4'' \pm 1.4''$. For $\sim 67\%$ of the sources the displacement is $< 3''$ (see figure 1). These shifts are slightly worse than those found for the HELLAS2XMM 1dF sample (average displacement of $2.0'' \pm 1.4''$ and 80% of the sources within $3''$, Fiore et al. 2003), most likely because the average off-axis angle (and therefore the average Point Spread Function) of the sources in the second sample is higher than for the sources in the 1dF sample, due to the exclusion of the central parts of two fields (Mrk421 and A1835).

3. Optical spectroscopic redshifts and classification

Our main effort was that of starting to explore the region of high X/O values to obtain an optical spectroscopy as uniform as possible regarding the X-ray to optical flux ratio. This has been roughly achieved up to $X/O=40$,

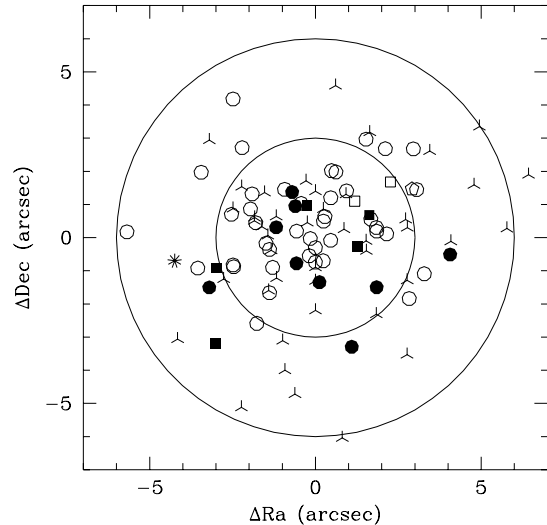


Fig. 1. The displacement between the X-ray position and the position of the nearest optical counterpart for the HELLAS2XMM second source sample. Open circles = broad-line AGN; filled circles = narrow-line AGN; filled squares = emission-line galaxies; open squares = early-type galaxies; stars = stars; pentagons = groups/clusters of galaxies; skeleton triangles = unidentified objects. The two circles have radii of 3 and 6 arcseconds, respectively.

which corresponds to $R \sim 24$ for 2–10 keV fluxes of $\sim 10^{-14} \text{ erg cm}^{-2} \text{ s}^{-1}$. Most of the HELLAS2XMM sources have X-ray flux higher than this figure.

Optical spectra of 59 out of the 110 sources with optical counterparts brighter than $R=24$ have been obtained using EFOOSC2 at the ESO 3.6m telescope, DOLORES at the TNG and FORS1 at the VLT/UT1 during 6 observing runs performed between August 2001 and March 2004. A total of 12 nights at the 3.6m and TNG telescopes and ~ 40 hours of VLT time have been devoted to this program.

Long slit spectroscopy has been carried out in the 3800–10000 Å band with resolution between 7 and 13 Å. Data reduction was performed using both the MIDAS (Banse et al. 1983) and IRAF³ packages. Wavelength calibrations were carried out by comparison with exposures of He-Ar, He, Ar and Ne lamps. The flux calibration of the spectra was obtained using observations of spectrophotometric standard stars (Oke, 1990) performed within a few hours from the spectroscopy of our sources.

Regardless of the optical spectra, our discriminant for supermassive black hole accretion is high X-ray luminosity; we classify a source as an AGN if it has an X-ray luminosity $\log L_{2-10\text{keV}} \geq 42$; if a source has an X-ray luminosity $\log L_{2-10\text{keV}} \geq 44$ we classify it as a QSO can-

² $P = e^{-\pi r^2 n(R)}$ where r is the X-ray–optical displacement and $n(R)$ the number counts of galaxies as a function of their magnitude from Metcalfe et al. (2001)

³ IRAF is distributed by the National Optical Astronomy Observatories, which is operated by the Association of Universities for Research in Astronomy, Inc., under cooperative agreement with the National Science Foundation.

didate. Following Fiore et al. (2003), objects with permitted emission lines broader than 2000 km/s (FWHM)⁴ are classified type 1 AGN or QSO; objects with permitted emission lines narrower than this threshold and strong (equivalent width $EW > 5 \text{ \AA}$) [OIII], MgII, NeV or CIV emission lines are classified type 2 AGN; objects with faint (equivalent width $EW < 5 \text{ \AA}$) [OIII] and/or strong [OII] or H α and no high ionization emission lines are classified Emission-Line Galaxies (ELGs). In one case the presence of broad emission lines in the optical spectrum cannot be excluded due to the insufficient quality of the spectrum and the classification of the object is therefore uncertain (see notes in Table 1). Objects without strong emission lines but with stellar absorption lines and a red continuum are classified as Early Type Galaxies (ETGs, or XBONGs as they are X-ray bright sources with optical spectra typical of early type galaxies). Table 1 gives for each source the classification of the optical spectrum, the redshift and the X-ray luminosity.

The source breakdown includes: 41 broad-line AGNs (QSOs and Seyfert 1 galaxies, $\log L_{2-10\text{keV}} > 44$ and $\log L_{2-10\text{keV}} < 44$, respectively); 9 narrow-line AGNs (type 2 QSOs and Seyfert 2 galaxies); 5 emission-line galaxies, all with $\log L_{2-10\text{keV}} > 42.7$ and therefore all probably hosting an AGN; 2 early-type galaxies, both with $\log L_{2-10\text{keV}} > 42.0$ and, therefore, XBONG candidates, probably hosting an AGN; 1 group of galaxies; 1 star. In summary, 57 of the 59 sources with optical spectroscopy are associated with AGN emission, the majority (69%) are type 1 AGNs. This brings the number of confirmed AGNs in the full HELLAS2XMM sample to 155 out of 159 with a spectroscopic redshift.

The four panels of figure 2 show the redshift-luminosity plane, and the redshift, R magnitude, X-ray-to-optical flux ratio histograms for the full HELLAS2XMM sample. The observed fraction of type 1 AGNs increases strongly with redshift, corresponding to $\sim 90\%$ of the *whole* source population with a spectroscopic redshift higher than 1.5. Conversely, the fraction of type 1 AGNs decreases strongly with increasing X-ray-to-optical flux ratio and with the magnitude of the optical counterpart of the X-ray source, with only one of the eleven sources with $R \gtrsim 23.3$ and a spectroscopic redshift identified as a type 1 AGN (see Fiore et al. 2003, La Franca et al. 2005, Eckart et al. 2006, Silverman et al. 2005, Treister et al. 2005, Steffen et al. 2004 for similar results and more detailed discussions). This suggests that the lack of high- z type 2 AGNs in the sample of spectroscopically identified HELLAS2XMM sources (Fig.2, upper right panel) can be probably due to the incompleteness of the sample: at $z \gtrsim 1.5$ the R-band magnitude of the optical counterparts of type 2 AGN is often beyond the spectroscopic limit of our sample ($R \sim 24$). Furthermore, even for objects brighter than the spectroscopic limit, the optical nucleus is so dim that the redshift

determination is complex for the lack of observable lines, the so called spectroscopic redshift desert at $z=1.5-2$.

3.1. Optically obscured AGN

Following Fiore et al. (2003), we limit ourselves to consider two broad AGN categories: optically unobscured AGN, i.e. type 1, broad emission line AGN, and optically obscured AGN, i.e. non type 1 AGN, in which the nuclear optical emission is totally or partly reduced by dust and gas in the nuclear region and/or in the host galaxy. The fraction of optically obscured AGN with respect to the total number of identified X-ray sources is approximately 27% (16 out of 59 X-ray sources, see also the source breakdown). Two examples of such sources are reported in figure 3. The H_β FWHM of GD153_236 (H2XMMJ125654.1+215318; $z=0.909$, AGN2) is $< 1000 \text{ km s}^{-1}$. Faint [OII] and [OIII] emission is present in the spectrum of A1835_262 (H2XMMJ140130.8+024532; $z=0.746$, ELG). The latter source is obscured also in the X-ray band, having a 0.5-2 keV flux less than 20 times the observed 2-10 keV flux; to be more quantitative, the X-ray spectral fit yields a rest frame $N_H(z) \simeq 7.9_{-2.2}^{+3.3} \times 10^{22} \text{ cm}^{-2}$, fixing the spectral energy index α_E ($F(E) \propto E^{-\alpha_E}$) to 0.9. GD153_236 is less extreme in this regard, the X-ray spectral fit yields a rest frame $N_H(z) = 0.3_{-0.3}^{+0.4} \times 10^{22} \text{ cm}^{-2}$, fixing the spectral energy index α_E to 0.9. The 2–10 keV intrinsic luminosity is $1.10 \times 10^{44} \text{ erg s}^{-1}$ for A1835_262 and $1.59 \times 10^{44} \text{ erg s}^{-1}$ for GD153_236, making them obscured QSO candidates.

We are interested in finding a statistical method to select highly obscured QSOs candidate among the still unidentified sample sources in order to estimate their surface density. To this purpose, in the following, we will make use of observed quantities, such as the observer-frame absorbing column N_H and the X/O ratio. We use the results of our spectroscopic identifications to calibrate and validate this statistical method.

The observed-frame absorbing column $N_H(z=0)$ (computed from the hardness ratios following Fiore et al. 2003) as a function of X/O for the full HELLAS2XMM sample is reported in figure 4 (left panel). We note that the part of the diagram at $X/O > 8$ and $\log N_H(z=0) > 21$ is populated mainly by narrow-line objects. More quantitatively, 16 out of the 20 objects with optical spectroscopy are, according to the definition of Fiore et al. (2003), optically obscured AGNs (i.e., $80 \pm 20\%$).

Since the observed $\log N_H=21$ would correspond to a rest-frame column density of $\log N_H = 21.5$ at $z=1$, most of these AGNs, having redshifts $z \gtrsim 1$, are also X-ray obscured (see also Mainieri et al. 2002). The right panel of figure 4 shows X/O as a function of the 2-10 keV luminosity for the HELLAS2XMM full source sample. This figure clearly shows that most optically obscured AGN with $X/O > 8$ have high-luminosities ($\log L(2-10 \text{ keV}) > 44$), highlighting the efficiency of a selection based on the observed X/O ratio to find highly obscured QSO candidates. The number of spectroscopically identified sources in the

⁴ Removing the instrumental broadening from the line profile, the adopted velocity threshold corresponds to an intrinsic FWHM of $\sim 1500 \text{ km/s}$.

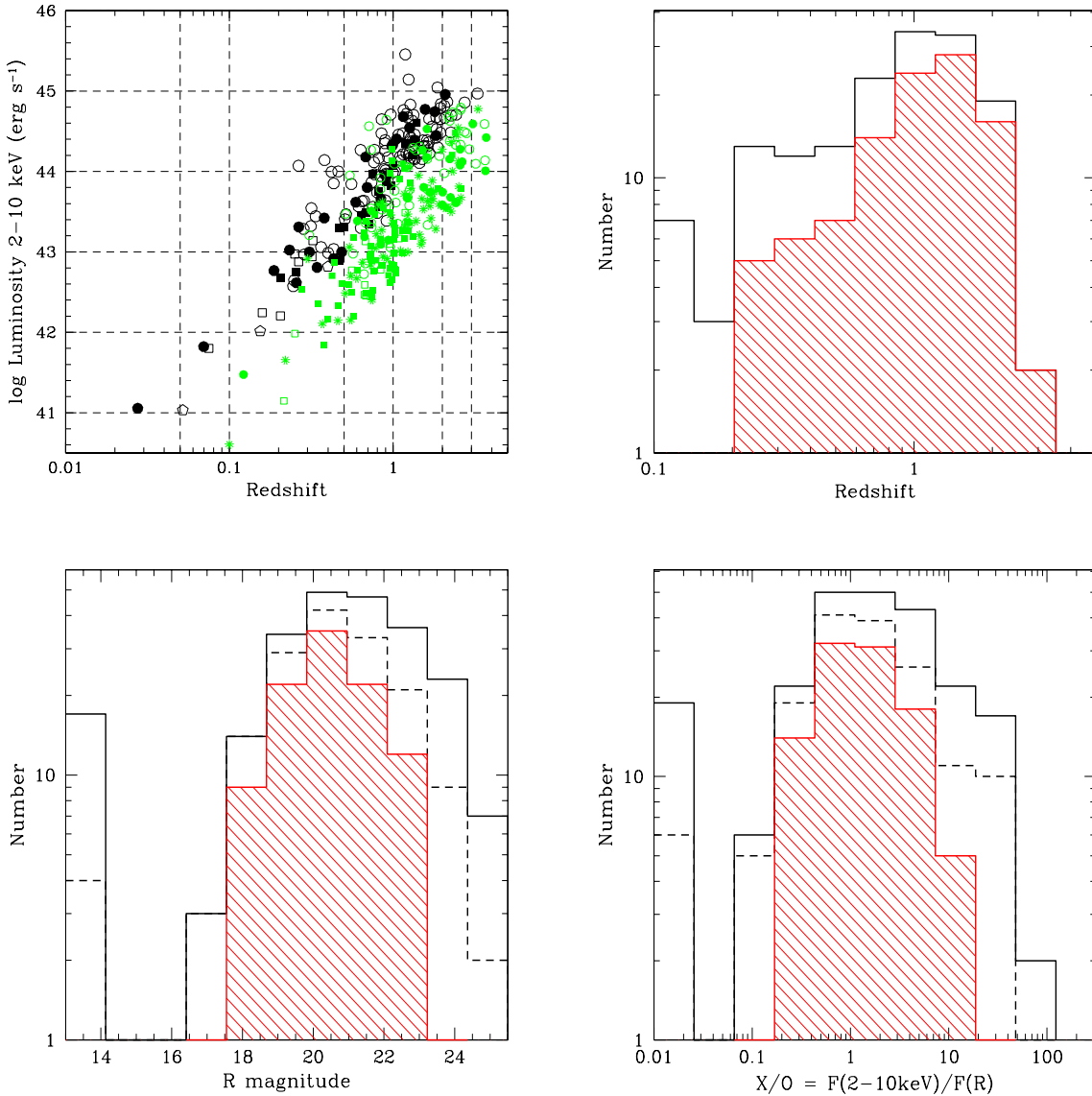


Fig. 2. a) Upper left panel: the 2-10 keV luminosity as a function of the redshift for the sources in the full HELLAS2XMM sample (black points) compared with the luminosity as a function of the redshift for CDFFS+CDFN samples (smaller green points; data from Giacconi et al. 2002, Alexander et al. 2003, Barger et al. 2003, Szokoly et al. 2004). Stars are CDFFS and CDFN sources with photometric redshifts. b) upper right panel: the redshift distribution of the 159 sources with spectroscopic redshifts of the full HELLAS2XMM sample. The hatched histogram refer to type 1 AGN only and the continuous histogram to the source population with spectroscopic z . c) lower left panel: the R magnitude distribution; d) lower right panel: the X-ray to optical flux ratio X/O distribution. In the c) and d) panels the hatched histograms refer to type 1 AGN only, the dashed histograms to the source population with spectroscopic z , the continuous histograms to the whole source population.

HELLAS2XMM sample with $\log N_H(0) > 21$, $X/O > 8$ and $\log L(2-10 \text{ keV}) > 44$ is 17. 13 of these are optically obscured AGN, i.e. a fraction of 0.76 ± 0.25 .

The diagram in the left panel of figure 5 shows the $N_H(0)$ as a function of X/O ratio for the CDFFS and CDFN sources (Giacconi et al. 2002, Alexander et al. 2003, Barger et al. 2003, Szokoly et al. 2004) selected by Fiore (2004) by having 2-10 keV fluxes larger than $10^{-15} \text{ erg cm}^{-2} \text{ s}^{-1}$ and off axis angles lower than 10 arcmin.

Unfortunately, most of the sources from these samples with $X/O > 8$ and $\log N_H(z=0) > 21$ do not have a spectroscopic redshift⁵: in the following analysis we will assume

⁵ As regard the optical classification of the CDFFS and CDFN identified sources we applied, where possible, our classification criteria. The X-ray fluxes are taken from Alexander et al. (2003). The catalog reports 2-8 keV fluxes converted to 2-10 keV fluxes using a power-law model with spectral energy index $\alpha_E = 0.8$.

that the fraction of optically obscured AGN in these faint sources is similar to the fraction in the HELLAS2XMM sample, i.e. a fraction of $0.76^{+0.25}$. Assuming the fraction of optically obscured QSOs, it is possible to compute their integral number counts relations which are compared with the logN–logS of the entire samples in figure 5b). Number counts and relative sky coverages are also tabulated in Table 2.

The line of reasoning followed to compute the fraction of optically obscured QSOs implies that the Fiore et al. (2003) relationship between X/O and log L(2–10 keV) may be directly applicable to the CDFS and CDFN sources with the faintest optical counterparts, assuming that also these sources are very likely high-luminosity objects, including them among the optically obscured QSO population. However, Bauer et al. (2004) and Barger et al. (2005) pointed out that the Fiore et al. (2003) relationship could not be valid at faint ($R > 25.5$) optical magnitudes. For this reason, we re-computed the optically obscured QSO number counts by excluding all X-ray sources with optical counterparts fainter than $R=25.5$ (open triangles in figure 5b). This is probably a lower limit to the “true” type 2 QSO surface density. In summary, we find a highly obscured QSO density of 45 ± 15 and $100\text{--}350 \text{ deg}^{-2}$ at flux limits of 10^{-14} and $10^{-15} \text{ erg cm}^{-2} \text{ s}^{-1}$, respectively (see figure 5b). The fraction of obscured QSOs to the total number of X-ray sources selected in the 2–10 keV band is therefore $\sim 13\%$ and between 4–14% at the two flux limits.

3.2. X-ray Bright Optical Normal Galaxies

In figure 6 we show the R-band images of the XBONG candidates with the largest X-ray to optical position difference. Superimposed are the X-ray position error boxes (3” and 6” black circles) and the X-ray contours (grey). Close to the X-ray position of A1835_140 there are 2 optically bright sources, one within 3” from the X-ray centroid and the other at 6.6”; both sources are clearly extended and their morphology is consistent with a spheroid. No optical point-like nucleus is evident in both sources (see, also, Civano et al. 2006, in preparation).

The X-ray contours are well centered on the source we identified as the optical counterpart of the X-ray source. The R-band images of PKS0312_17 (H2XMMJ031124.8-770139) and PKS0312_501 (H2XMMJ030952.2-764927) are reported in the bottom panels; the optical counterpart identified for PKS0312_17 lies at 4.6” from the nominal X-ray centroid but it is coincident with a relatively bright radio source (the square refers to the radio centroid, 4” width, see Brusa et al. 2003 for details). We therefore consider this optical source as the most likely counterpart of the X-ray source. As we can see in fig. 6, the X-ray centroid of PKS0312_501 provided by the detection algorithm is slightly shifted from the peak of the X-ray contours, which is coincident with the optical counterpart. We therefore consider as reliable also this identification.

A paper discussing in more detail these sources and presenting near-infrared imaging is in preparation (Civano et al. 2006). As an example, figure 7 shows the spectra of 2 XBONGs, which we tentatively classify as early-type galaxies based on the strong red continuum and the absence of emission lines (however, note that these spectra do not cover the $H\alpha$ transition).

3.3. [OIII] λ 5007 emission

For 59 of the 159 optical spectra of the full HELLAS2XMM sample the [OIII] λ 5007 line falls in the observed wavelength range. We measured⁶ significant [OIII] λ 5007 emission in 49 cases: 26 broad-line AGNs, 23 narrow-line AGNs (including 8 objects with optical spectra classified as emission-line galaxies but with 2–10 keV luminosity higher than $10^{42} \text{ erg s}^{-1}$). In the remaining 10 cases, 7 candidate XBONGs and 3 galaxies belonging to groups or small clusters of galaxies, we computed the 3σ upper limits (see Table 3).

Figure 8a) shows the [OIII] λ 5007 flux as a function of the 2–10 keV flux, while figure 8b) shows the rest-frame N_H (computed using flux ratios, see Fiore et al. 2003) as a function of the ratio between the 2–10 keV and the [OIII] λ 5007 luminosities for the 59 objects. Note that the XBONG candidates, in figure 8a), have systematically lower [OIII] fluxes compared with other sources with the same X-ray flux and have $L_{2-10\text{keV}}/L_{[\text{OIII}]}\gtrsim 1000$. The only other HELLAS2XMM AGN with a X-ray-to-[OIII] luminosity ratio well above this value is the broad line AGN A2690_3, a Seyfert 1 galaxy at $z=0.433$ with a strong broad MgII and $H\beta$ lines but very faint [OIII] emission⁷. Other three HELLAS2XMM AGN have $L_{2-10\text{keV}}/L_{[\text{OIII}]}\sim 1000$. This suggests that AGNs with small [OIII] emission are probably more common than what was thought before and the the XBONGs are the tip of the iceberg of these source population.

4. Discussion

The hard X-ray selection and the good photometric and spectroscopic coverage of the ten HELLAS2XMM fields allow us to probe AGN activity over a wide range of broad band properties. In this paper we focus our attention on two extremes of the AGN activity: on one side, sources with high X-ray-to-optical flux ratio, the majority of which turned out to be the so far “elusive” high-luminosity, highly obscured type 2 QSOs; on the other side, sources with relatively low X-ray-to-optical flux ratios, moderately luminous ($L_X \simeq 10^{42-43} \text{ erg s}^{-1}$) active nuclei in otherwise inactive galaxies, the so called XBONGs.

⁶ The [OIII] λ 5007 fluxes were measured performing a Gaussian fit of the line using the standard IRAF task *splot*.

⁷ See <http://www.bo.astro.it/~hellas/sample.html>

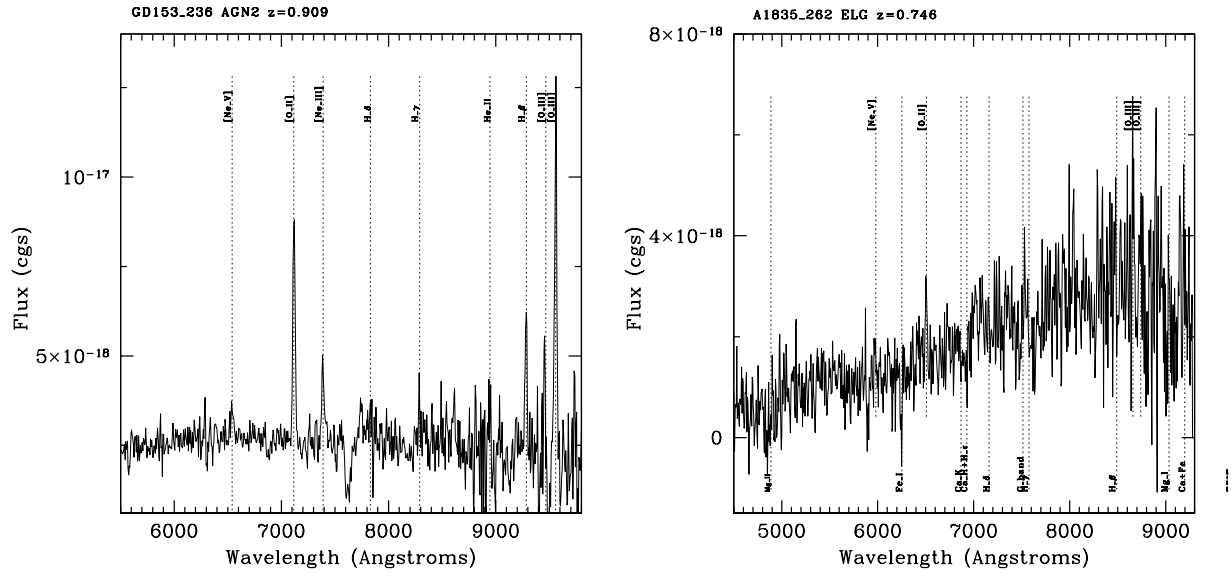


Fig. 3. The optical spectra of GD153_236 (H2XMMJ125654.1+215318) and A1835_140 (H2XMMJ140130.8+024532). Both spectra are classified as narrow emission-line objects based on the H_β FWHM (< 1000 km s $^{-1}$, GD153_236), narrow [OII] and [OIII] emission, absence of broad permitted lines (A1835_140), and high 2-10 keV luminosity ($\sim 10^{44}$ erg s $^{-1}$ for both sources).

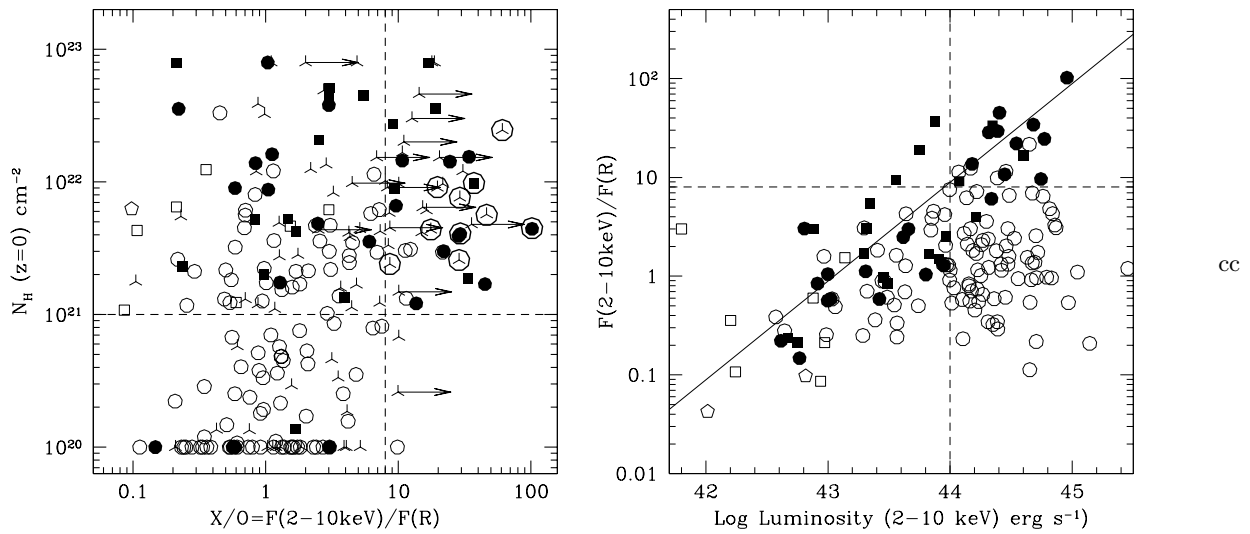


Fig. 4. The observed-frame absorbing column $N_H(z=0)$ as a function of the X-ray (2-10 keV) to optical (R-band) flux ratio X/O (left panel) and the X/O ratio as a function of the 2-10 keV luminosity (right panel) for the HELLAS2XMM full sample. Open circles = broad-line AGN; filled circles = narrow-line AGN; filled squares = emission-line galaxies; open squares = early-type galaxies; pentagons = groups/clusters of galaxies; skeleton triangles = unidentified objects. The 10 encircled symbols in the left panel have extreme R-K colors (R-K > 5, see Mignoli et al. 2004). The diagonal line, in the right panel, is the best linear regression between $\log(X/O)$ and $\log L(2-10 \text{ keV})$ (from Fiore et al. 2003). The dashed lines represent the loci of constant $N_H = 10^{21}$ cm $^{-2}$, X/O=8 and $\log L(2-10 \text{ keV})=44$.

4.1. The high X/O flux ratio sources

As far as the first topic is concerned, we confirm the finding that about 20% of hard X-ray selected sources have an X-ray-to-optical flux ratio which is, on average, one order of magnitude or more higher than that

of optically selected AGNs. Our spectroscopic identifications suggest that $\sim 76\%$ of the sources with X/O > 8 and $\log N_H(z=0) > 21$ are highly obscured QSOs at $z=0.7-2$ (see also Table 1). This implies a number density of optically obscured QSOs of ~ 45 deg $^{-2}$ at a flux limit of 10^{-14}

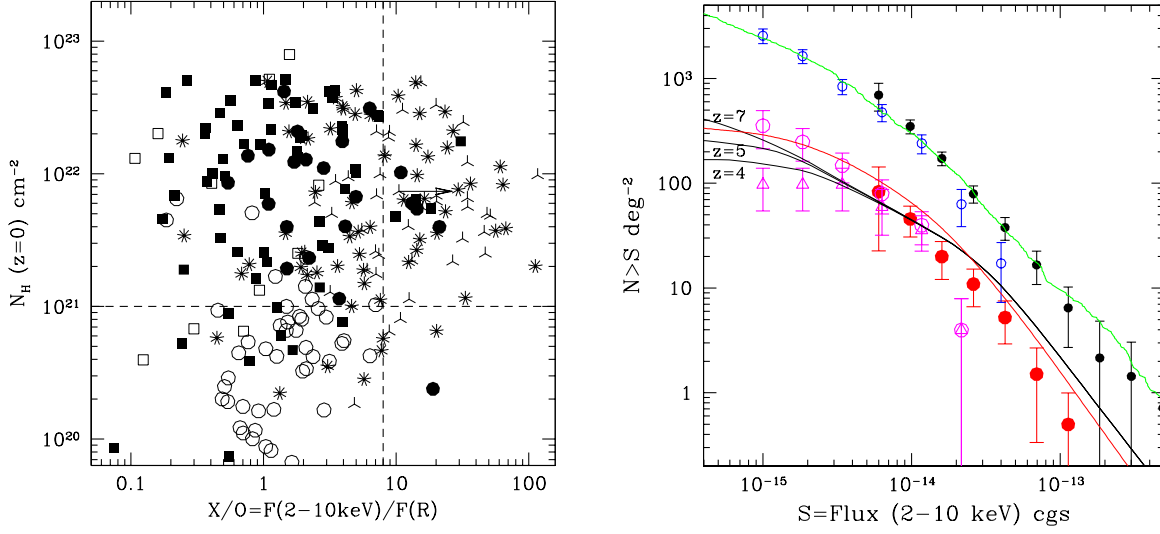


Fig. 5. a) Left panel: the observed-frame absorbing column $N_H(z=0)$ as a function of the X-ray (2-10 keV) to optical (R-band) flux ratio X/O for the CDFS and CDFN samples. Open circles = broad-line AGN; filled circles = narrow-line AGN; filled squares = emission-line galaxies; open squares = early-type galaxies; pentagons = groups/clusters of galaxies; skeleton triangles = unidentified objects. The stars are sources with a photometric redshift. The dashed lines represent the loci of constant $N_H = 10^{21} \text{ cm}^{-2}$ and $X/O=8$. b) right panel: the X-ray (2-10 keV) integral number counts from the HELLAS2XMM (filled symbols) and CDF+CDFN samples (open symbols). The upper points are the number counts of the full samples, the solid curve is from the Moretti et al. (2003) compilation. The lower points refer to high-luminosity ($\log L(2-10 \text{ keV}) > 44$), highly obscured sources only. Open triangles include only sources with optical counterparts brighter than $R=25.5$. Black continuous lines represent the expected number counts from the Comastri et al. (2001) pure luminosity evolution XRB synthesis models ($z=4, 5, 7$ are the maximum redshift over which the integration of the XLF is performed); the red line represents the expected number counts from the La Franca et al. (2005) luminosity dependent density evolution model.

Table 2. Number counts and sky coverage

F(2-10 keV) ($10^{-14} \text{ erg cm}^{-2} \text{ s}^{-1}$)	Sky-coverage (deg^2)	Tot. N.C. (deg^{-2})	QSO2 N.C. (deg^{-2})	QSO2 N.C.($R < 25.5$) (deg^{-2})
HELLAS2XMM				
11.3	1.39	5.7 ± 2.8	0.5 ± 0.5	
6.93	1.37	16 ± 5.1	1.6 ± 1.4	
4.25	1.25	38 ± 8.7	5.7 ± 3.1	
2.60	0.98	79 ± 15	12.0 ± 6.1	
1.60	0.5	170 ± 26	21.9 ± 11.3	
0.98	0.11	350 ± 53	50.1 ± 23.2	
0.60	0.015	700 ± 210	91.1 ± 73.0	
CDFS+CDFN				
4.00	0.174	17 ± 9.9	-	-
2.16	0.174	63 ± 24	4.3 ± 4.6	4.3 ± 4.6
1.17	0.174	240 ± 50	43 ± 21	39 ± 19
0.63	0.174	475 ± 89	87 ± 43	65 ± 37
0.34	0.14	840 ± 140	162 ± 74	106 ± 58
0.18	0.07	1640 ± 250	272 ± 130	106 ± 58
0.10	0.06	2560 ± 410	388 ± 200	106 ± 58

$\text{erg cm}^{-2} \text{ s}^{-1}$. Within the reasonable hypothesis that the fraction of obscured QSOs among the sources with $X/O > 8$ and $\log N_H(z=0) > 21$ remains constant down to fluxes of $10^{-15} \text{ erg cm}^{-2} \text{ s}^{-1}$, an obscured QSOs density of $\sim 350 \text{ deg}^{-2}$ is implied. A much more conservative estimate of

the obscured QSO space density ($\sim 100 \text{ deg}^{-2}$ at $10^{-15} \text{ erg cm}^{-2} \text{ s}^{-1}$), which should probably be considered as a lower limit, is obtained assuming that all sources with optical counterparts fainter than $R=25.5$ have X-ray luminosities below the highly obscured QSO threshold.

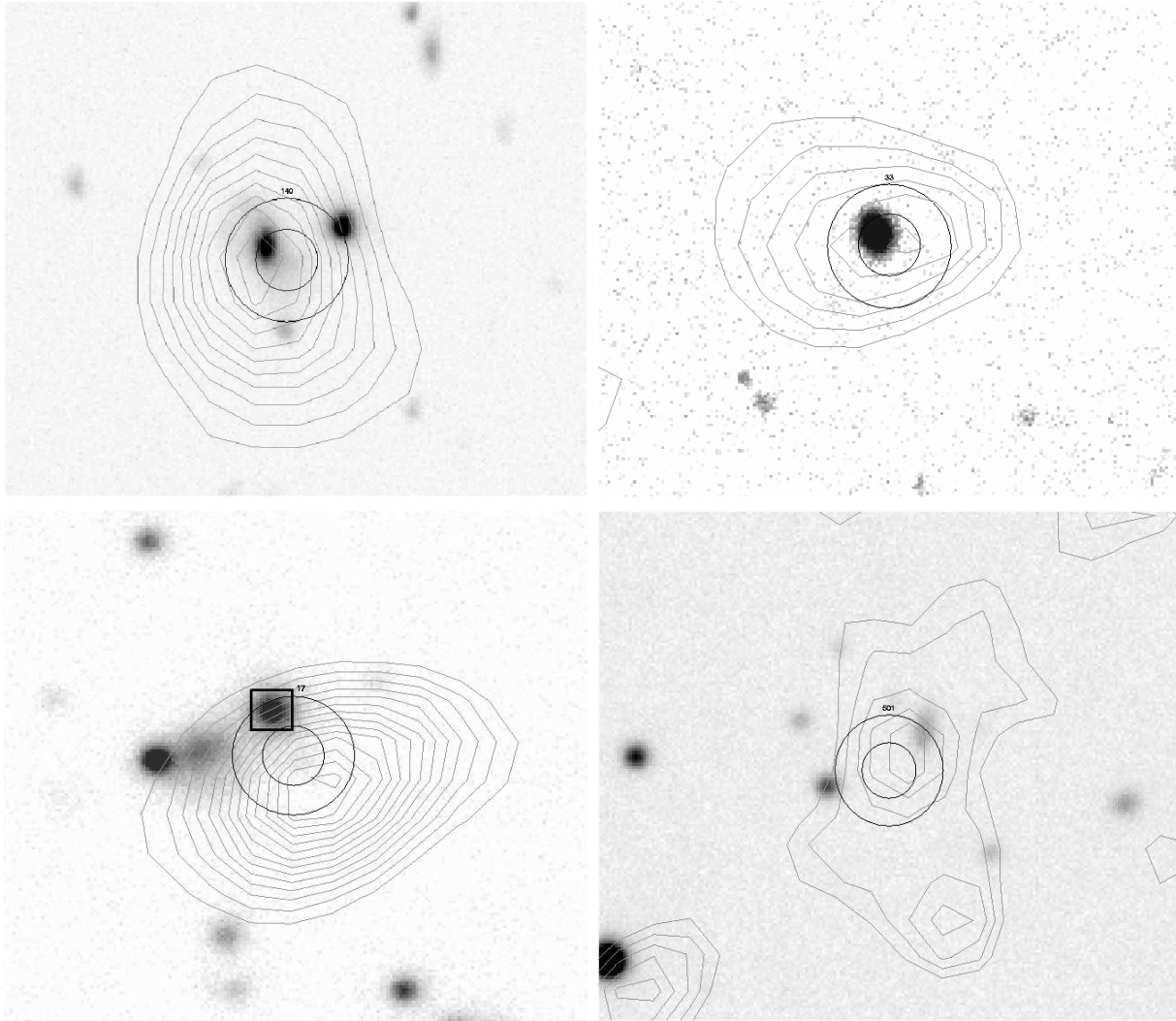


Fig. 6. Upper panels: the R-band images of A1835_140 (H2XMMJ140144.9+025332, left) and A1835_33 (H2XMMJ140057.3+023942, right): superimposed are the X-ray position error boxes (3" and 6" black circles) and the X-ray contours (grey). The X-ray contours are well centered on the sources identified by us as the optical counterpart of the X-ray sources. Bottom panels: the R-band images of PKS0312_17 (H2XMMJ031124.8-770139, left) and PKS0312_501 (H2XMMJ030952.2-764927, right): the optical counterpart identified for PKS0312_17 is coincident with a relatively bright radio source (the square refers to the radio centroid, 4" width, see Brusa et al. 2003). The X-ray centroid of PKS0312_501 is slightly shifted from the peak of the X-ray contours, which are coincident with the optical counterpart. We therefore consider also this identification as reliable.

The three black solid curves in figure 5b) superimposed to the number counts of high-luminosity, highly obscured objects from both HELLAS2XMM and CDFS+CDFN samples are the number counts of obscured QSO predicted by the Comastri et al. (1995, 2001) XRB synthesis models. These models assume an evolution of the X-ray luminosity function parameterized by a pure luminosity evolution (PLE) law [$L(z) \propto L(z = 0) \times (1 + z)^{2.6}$] up to $z = 1.5$ and constant up to a maximum redshift z_{max} ($z_{max}=4,5,7$; see figure 5b). These predictions (depending also on the adopted maximum redshift) lie in between the two number counts obtained assuming that 70% of the high X/O sources are obscured QSOs or including in the obscured QSO sample sources with optical coun-

terparts brighter than $R=25.5$ only, respectively. The red curve in the figure 5b) represents the prediction obtained by the luminosity dependent density evolution (LDDE) model of the hard X-ray luminosity function described in La Franca et al. (2005). Not surprisingly, the shape of the number counts relations obtained by integrating the PLE and the LDDE models are different. The latter slightly overpredicts the highly obscured QSO number counts at fluxes $\gtrsim 10^{-14}$ erg cm $^{-2}$ s $^{-1}$, while at lower fluxes agrees pretty well with the expectations based on the identification of obscured QSOs with 70% of the high X/O sources (see Section 3.1). The same model predicts that the number of obscured QSO with $\log L(2-10\text{keV}) > 44$ is comparable to that of unobscured QSO. A similar conclusion was

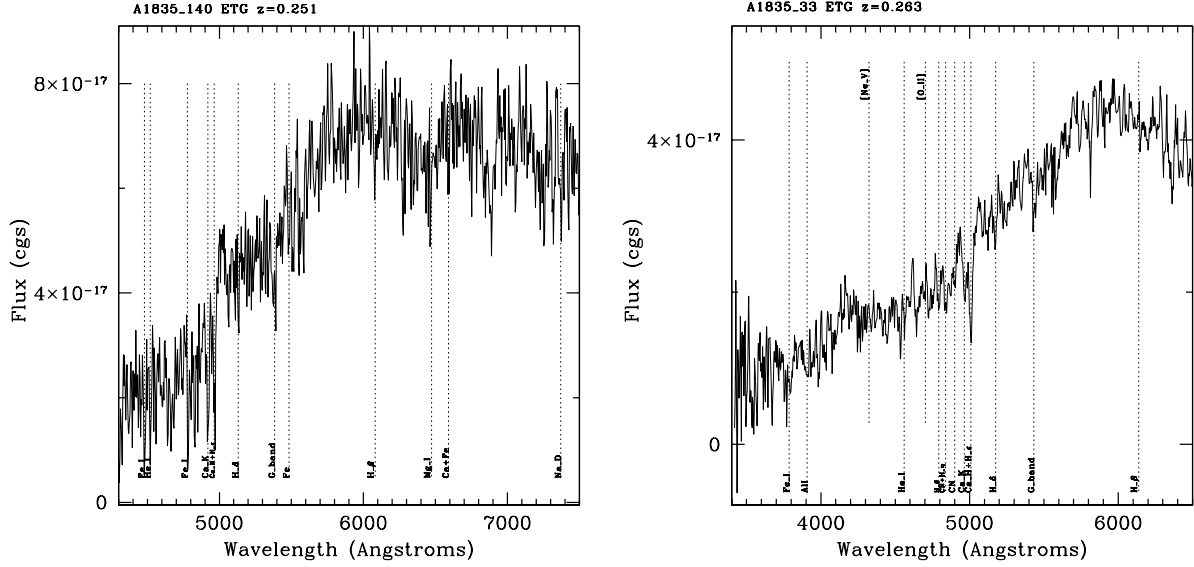


Fig. 7. The optical spectra of A1835_140 (H2XMMJ140144.9+025332, $z=0.251$) and A1835_33 (H2XMMJ140057.3+023942, $z=0.263$). Note the strong Balmer breaks, red continua and absence of strong [OII] and [OIII] emission lines.

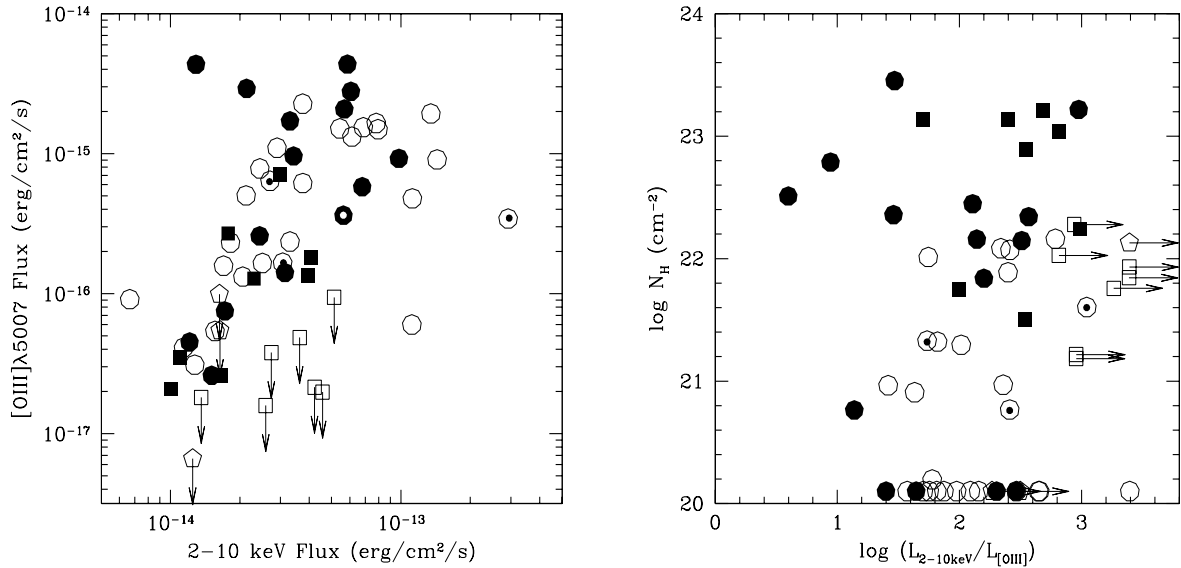


Fig. 8. a) Left panel: the [OIII] λ 5007 flux as a function of the 2-10 keV flux for 59 sources of the full HELLAS2XMM sample. b) Right panel: the rest-frame absorbing column density N_H (computed using flux ratios) as a function of the ratio between the 2-10 keV luminosity and the [OIII] λ 5007 luminosity. Open circles = broad-line AGN; filled circles = narrow-line AGN; filled squares = emission-line galaxies; open squares = early-type galaxies; pentagons = groups/clusters of galaxies; skeleton triangles = unidentified objects. The four encircled symbols in both panels mark objects for which the [OIII] λ 5007 line lies within strong telluric absorption features.

found by Perola et al. (2004) using a smaller source sample (the HELLAS2XMM 1dF sample). However, most of these hard X-ray selected highly obscured QSOs have column densities in the range $N_H \sim 10^{22-23} \text{ cm}^{-2}$ with only a handful of the faintest sources which could be Compton thick ($N_H > 10^{24} \text{ cm}^{-2}$). According to the most recent

version of the AGN synthesis models for the X-ray background (Gilli et al. 2006), the fraction of Compton-thick AGN in deep XMM-Newton and Chandra surveys is expected to be at most a few percent. Indeed, Tozzi et al. (2006) find that only about 4% of the sources in the CDFS have a 0.5–8 keV spectrum consistent with Compton-thick

absorption and/or pure reflection. Therefore, we still may be viewing just the tip of the iceberg of highly obscured sources at high-redshift.

An approach to find highly obscured, Compton-thick, QSOs is to select sources with QSO luminosities in the mid-infrared band and faint or extremely faint near-infrared and optical counterparts. Martinez-Sansigre et al. (2005) estimate that probably more than half of the high-luminosity QSOs are highly obscured, although with large uncertainties. Unfortunately, the X-ray properties of infrared selected sources are not known, and therefore it is difficult to understand how the mid-infrared selection compares with the X-ray one. In particular, it is not clear what is the fraction of the mid-infrared selected highly obscured QSOs which would have been selected by hard X-ray surveys, and whether the mid-infrared selection is truly more efficient in discovering Compton-thick sources. To answer to these questions we can take advantage of the study of fields with both X-ray and mid-infrared coverage; for example, we have under analysis Spitzer observations of 12 HELLAS2XMM sources (Pozzi et al. in preparation). Furthermore, the study of the ELAIS-S1 (Puccetti et al. 2006) and the COSMOS fields, and/or deep X-ray follow-up observations of the mid-infrared selected sources in the Spitzer First Look Survey (Martinez-Sansigre et al. 2005) will certainly bring new light on this topic.

4.2. XBONGs

At the other extreme of the X-ray-to-optical flux ratio distribution, we find the other class of “elusive” AGN (i.e., XBONGs), objects which have Seyfert-like X-ray luminosities but without any signature of nuclear activity in either optical imaging or spectroscopy (Comastri et al. 2002; Moran et al. 2002; Severgnini et al. 2003). In order to provide a quantitative definition of these objects, the flux and luminosity of the [OIII] λ 5007 emission (or their upper limits) are measured for the 59 spectra in the full HELLAS2XMM sample that cover this transition. The HELLAS2XMM AGNs with [OIII] detection have a $L_{2-10\text{keV}}/L_{[\text{OIII}]}$ ratio between 3 and 1000 with a logarithmic median and interquartile range of 2.14 ± 0.38 . This is systematically higher than optically selected sources. As an example, unobscured PG quasars at $z < 0.4$ have $L_{2-10\text{keV}}/L_{[\text{OIII}]}$ in the range 6-500 (Laor et al. 1997), Compton thin, Seyfert 2 galaxies have $L_{2-10\text{keV}}/L_{[\text{OIII}]}$ between 3 and 50 while Compton-thick Seyfert 2 galaxies have $L_{2-10\text{keV}}/L_{[\text{OIII}]}$ between 0.03 and 1 (Maiolino et al. 1998, Bassani et al. 1999). All the HELLAS2XMM AGNs have $L_{2-10\text{keV}}/L_{[\text{OIII}]} > 3$ and therefore, as discussed above, no Compton-thick object ($\log N_H \gtrsim 24$) is likely to be present in the HELLAS2XMM sample. The discrepancy between the $L_{2-10\text{keV}}/L_{[\text{OIII}]}$ ratio of the HELLAS2XMM AGN and optically selected AGNs could be due to the fact that the [OIII] luminosity of the HELLAS2XMM AGN is not corrected for reddening. This correction can be very large for highly obscured sources.

Indeed, the typical correction in Bassani et al. (1999) is a factor between 2 and 10, with a few extreme objects with a correction approaching 50. The logarithmic median $L_{2-10\text{keV}}/L_{[\text{OIII}]}$ and its interquartile range of a sample of 24 Compton thin, narrow line AGN from the catalogs of Maiolino & Rieke (1995) and Bassani et al. (1999), obtained without correcting for extinction, plus 17 PG quasar from the Laor et al (1997) sample (41 sources in total), is 1.69 ± 0.30 , lower than the median of the HELLAS2XMM sources. The probability that the two $\log L_{2-10\text{keV}}/L_{[\text{OIII}]}$ distributions are drawn from the same parent population is 1.8%, using the Kolmogorov-Smirnov test. The higher $L_{2-10\text{keV}}/L_{[\text{OIII}]}$ ratio of X-ray selected AGN with respect to optically selected AGN is intriguing, because it suggests that the latter samples are at least partly incomplete, and that [OIII] emission is not a perfect isotropic indicator of the nuclear power. However, this must be confirmed by using larger samples with both good X-ray and [OIII] determinations.

Narrow-line AGNs tend to have higher column densities than broad-line AGNs, but we do not see any correlation between the column density and $L_{2-10\text{keV}}/L_{[\text{OIII}]}$ (see figure 8b). On the other hand, XBONG candidates have lower [OIII] fluxes compared with the other sources with similar X-ray flux (see figure 8a) and have $L_{2-10\text{keV}}/L_{[\text{OIII}]} \gtrsim 1000$ (see figure 8b). This suggests that the $L_{2-10\text{keV}}/L_{[\text{OIII}]}$ ratio is a robust index to define X-ray bright but optically normal galaxies (XBONGs), at least in the X-ray and [OIII] flux ranges covered by the present observations. Note that this classification criterion is nearly independent by the galaxy dilution of the nuclear spectrum, which has been suggested to be a key ingredient in the classification of XBONGs (see Severgnini et al. 2003, Moran et al. 2002, Georgantopoulos & Georgakakis 2005), since it is related to a direct measurement of the line flux and not to its equivalent width. Indeed, the main issue about the XBONGs nature is whether they are just typical AGNs (in terms of both X-ray and line emission luminosity) or, rather, they represent a truly distinct class. Our results strongly point towards the latter hypothesis.

To further investigate this issue, we compared the 7 XBONG candidates to 7 narrow-line AGNs found in the same redshift interval (0.075–0.32). XBONGs and narrow-line AGNs have very similar X-ray luminosity (median $\log L(2-10 \text{ keV}) = 42.94$ vs. 42.76), optical luminosity (median $L(R) = 10.60$ vs. 10.77 L_\odot), X-ray-to-optical flux ratio (median X/O = 0.35 vs. 0.26) and absorbing column densities (median $\log N_H = 21.8$ vs. 21.6). On the other hand, while the narrow-line AGNs have median [OIII] λ 5007 flux and luminosity of 9.2×10^{-16} erg $\text{cm}^{-2} \text{ s}^{-1}$ and 1.6×10^{41} erg s^{-1} , XBONGs have 3σ upper limits in the ranges $1.5 - 9.4 \times 10^{-17}$ erg $\text{cm}^{-2} \text{ s}^{-1}$ and $2.5 \times 10^{38} - 1.4 \times 10^{40}$ erg s^{-1} , i.e., 10–50 times lower than narrow-line AGNs. The above findings suggest that while the central engine of narrow-line AGNs and XBONGs is likely to be the same, narrow emission lines in XBONGs are strongly inhibited or obscured.

At least three possibilities are envisaged to explain the lack of optical line emission:

- 1) the physical size of the narrow emission-line region could be reduced with respect to normal AGNs, or even absent (see, e.g., Hawkins 2004)
- 2) the optical-UV nuclear continuum could be screened by circumnuclear absorbing gas and dust covering a large solid angle at the nuclear engine, so that the ionizing radiation does not (or only partially) reach the narrow emission-line clouds;
- 3) the emission lines could be quenched by obscuring dust spatially distributed on larger scales (i.e., kpc dust lanes) as observed in HST images of nearby Seyfert 2 galaxies (Malkan et al. 1998)

To disentangle between these hypotheses, we are pursuing an intensive multiwavelength observing strategy, including further high angular resolution X-ray imaging with *Chandra*, and spatially resolved optical spectroscopy with the VIMOS Integral Field Unit at VLT.

5. Conclusions

We have obtained optical photometry and spectroscopy for a sample of 110 sources detected in the 2–10 keV band in five additional XMM–*Newton* fields of the HELLAS2XMM serendipitous survey, covering additional 0.5 deg^2 of the sky at the bright flux limit (see Table 2). We report the spectroscopic identification of 59 new redshifts, bringing to 159 the total number of X-ray sources with redshift identifications in the full HELLAS2XMM sample (including the three near-infrared spectroscopic redshifts reported by Maiolino et al. 2006).

Combining the redshift information of the HELLAS2XMM sample with that available in the CDFS and CDFN surveys, the fraction of highly obscured type 2 QSOs is estimated to be of the order of $\sim 13\%$ of the total, rather independent from the X-ray flux for $F(2-10 \text{ keV}) > 10^{-15} \text{ erg cm}^{-2} \text{ s}^{-1}$. This result is in rough agreement with the Comastri et al. (2001) and La Franca et al. (2005) models and implies that about half of the luminous AGNs ($\log L(2-10\text{keV}) > 44$) are obscured.

We find that the 7 XBONG candidates in the full HELLAS2XMM sample have $L_{2-10\text{keV}}/L_{[\text{OIII}]} \gtrsim 1000$, while all but one of the other HELLAS2XMM AGNs have an X-ray-to-[OIII] ratio well below this value.

Although the sample is very small and, therefore, subject to large uncertainties, our results suggest that this ratio can be used to efficiently select XBONG candidates. Multiwavelength works with further surveys are needed to strengthen this result.

This research has been partially supported by ASI, INAF–PRIN 270/2003 and MIUR Cofin-03-02-23 grants. We acknowledge an anonymous referee for comments that improved the presentation. We thanks L. Pentericci, P. Tozzi and P. Severgnini for useful discussions.

References

- Alexander, D. M., Bauer, F. E., Brandt, W. N. et al. 2003, *AJ*, 126, 539
- Baldi, A., Molendi, S., Comastri, A. et al. 2002, *ApJ*, 564, 190
- Banse, K., Crane, P., Grosbol, P. et al. 1983, *The Messenger*, 31, 26
- Bassani, L., Dadina, M., Maiolino, R. et al. 1999, *ApJS*, 121, 473
- Barger, A. J., Cowie, L. L., Capak, P. et al. 2003, *AJ*, 126, 632
- Barger, A.J., Cowie, L.L., Mushotzky, R.F. et al. 2005, *AJ*, 129, 578
- Bertin, E. & Arnouts, S. 1996, *A&AS*, 117, 393
- Bauer, F. E., Alexander, D. M., Brandt, W. N. et al. 2004, *AJ*, 128, 2048
- Brandt, W.N., Hasinger, G. 2005, *ARA&A*, 43, 1056
- Brusa, M., Comastri, A., Mignoli, M., et al. 2003, *A&A*, 409, 65.
- Civano et al. in preparation
- Comastri, A., Setti, G., Zamorani, G., & Hasinger, G. 1995, *A&A*, 296, 1
- Comastri, A., Fiore, F., Vignali, C. et al. 2001, *MNRAS*, 327, 781
- Comastri, A., Mignoli, M., Ciliegi, P. et al. 2002, *ApJ*, 571, 771
- Comastri, A. 2004, in "Supermassive Black Holes in the Distant Universe", Ed. A. J. Barger, Kluwer Academic, vol. 308, p.245
- Croom, S. M., Boyle, B. J., Loaring, N. S. et al. 2002 *MNRAS*, 335, 459
- Della Ceca, R., Maccacaro, T., Caccianiga, A. et al. 2004, *A&A*, 428, 383
- Eckart, M.E., Laird, E.S., Stern, D. et al. 2005, *ApJS*, 156, 35
- Eckart, M.E., Stern, D., Helfand, D. et al. 2006, *ApJS*, 165, 19
- Fiore, F., La Franca, F., Vignali, C. et al. 2000, *NewA*, 5, 143
- Fiore, F., Brusa, M., Cocchia, F. et al. 2003, *A&A*, 409, 79
- Fiore, F. 2004, *NuPhS*, 132, 69
- Georgakakis, A. et al. 2004, *MNRAS*, 349, 135
- Georgantopoulos, I. & Georgakakis, A. 2005, *MNRAS*, 358, 131
- Giacconi, R., Zirm, A., Wang, J., et al. 2002, *ApJS*, 139, 369
- Gilli R., Comastri A., Hasinger G. *A&A*, submitted
- Hasinger, G., Burg, R., Giacconi, R. et al. 1998, *A&A*, 329, 482
- Hasinger, G. 2003, proceedings of the Conference: The Emergence of Cosmic Structure, Maryland, Stephen S. Holt and Chris Reynolds (eds), astro-ph/0302574
- Hawkins, M.R.S. 2004, *A&A* 424, 519
- Kauffmann, G., Heckman, T. M., Tremonti, C. et al. 2003, *MNRAS*, 346, 1055
- La Franca, F., Fiore, F., Comastri A. et al. 2005, *ApJ*, 635, 864
- Laor, A., Fiore, F., Elvis, M. et al. 1997, *ApJ*, 477, 93
- Maccacaro, T., Gioia, I., Wolter, A. et al. 1988, *ApJ*, 326, 680
- Mainieri, V., Bergeron, J., Hasinger, G., Lehmann, I., Rosati, P., Schmidt, M., Szokoly, G., & Della Ceca, R. 2002, *A&A*, 393, 425
- Maiolino, R. & Rieke, G.H 1995, *ApJ*, 454, 95
- Maiolino, R., Salvati, M., Bassani, L. et al. 1998, *A&A*, 338, 781
- Maiolino, R., Mignoli, M., Pozzetti, L. et al. 2006, *A&A*, 445, 457
- Malkan, M.A., Gorjian, V., Tam, R. 1998, *ApJ*, 117, 25
- Martinez-Sansigre, A., Rawlings, S., Lacy, M. et al. 2005, *Nature*, 436, 666

- Mignoli, M., Pozzetti, L., Comastri, A. et al. 2004, *A&A*, 418, 827
- Mineo, T., Fiore, F., Laor, A. et al. 2000, *A&A*, 359, 471
- Moran, E.C., Filippenko, A.V., Chornock, R. 2002, *ApJ*, 579, L71
- Moretti, A., Campana, S., Lazzati, D., Tagliaferri, G. 2003, *ApJ*, 588, 696
- Perola, G. C, Puccetti, S., Fiore, F. et al. 2004, *A&A*, 421, 491
- Puccetti, S., Fiore, F., D'Elia, V. et al. 2006, *A&A*, 457, 501.
- Oke, J.B. 1990, *AJ*, 99, 1621
- Severgnini, P., Caccianiga, A., Braito, V. et al. 2003, *A&A* 406, 483
- Silverman, J.D., Green, P.J., Barkhouse, W.A. et al. 2005, *ApJ*, 618, 123
- Steffen, A. T., Barger, A. J., Capak, P. et al. 2004, *AJ*, 128, 1483
- Szokoly, G. P., Bergeron, J., Hasinger, G. et al. 2004, *ApJS*, 155, 271
- Tozzi, P., Gilli, R., Mainieri, V. et al. 2006, *A&A*, 451, 457
- Treister, E., Castander, F. J., Maccarone, T. J. et al. 2005, *ApJ*, 621, 104
- Ueda, Y., Takahashi, T., Ishisaki, Y., & Ohashi, T. 1999, *ApJ*, 524L, 11
- Worsley, M. A., Fabian, A. C., Barcons, X. et al. 2004, *MNRAS*, 352, L28
- Zakamska, N. L., Strauss, M. A., Krolik, J. H. et al. 2003, *AJ*, 126, 2125

Table 1. The HELLAS2XMM second source sample

Observation Id	X-ray Position (J2000)	Optical Position (J2000)	Offaxis (arcmin)	Δ (arcsec)	Prob	F(2-10 keV) (10^{-14} cgs)	R	Class.	z	$\log L_{2-10\text{keV}}$ (erg/s)
H2XMMJ140144.9+025332 ^a	14 01 44.9 +02 53 32	14 01 45.0 +02 53 34	11.0	2.8	0.9990	5.13	18.00	ETG	0.2506	42.97
		14 01 44.9 +02 53 25		6.6	0.9171	–	20.69	–	–	–
H2XMMJ140144.8+024845	14 01 44.8 +02 48 45	14 01 44.8 +02 48 40	11.8	4.8		1.86	24.50	–	–	–
H2XMMJ140139.6+025722	14 01 39.6 +02 57 22	14 01 39.5 +02 57 21	10.6	1.5		2.44	19.10	AGN1	0.2490	42.64
H2XMMJ140137.1+024604	14 01 37.1 +02 46 04	14 01 37.3 +02 46 06	11.5	4.3		2.19	20.07	–	–	–
H2XMMJ140132.1+025222	14 01 32.1 +02 52 22	–	7.9	–		1.08	$\gtrsim 23.0$	–	–	–
H2XMMJ140130.8+024532 ^a	14 01 30.8 +02 45 32	14 01 30.6 +02 45 31	10.7	3.1	0.9808	4.08	20.93	ELG	0.7456	43.97
		14 01 31.1 +02 45 31		4.8	0.7087	–	23.55	–	–	–
H2XMMJ140127.7+025607	14 01 27.7 +02 56 07	14 01 27.7 +02 56 06	7.4	0.7		57.0	19.70	AGN1	0.2645	44.07
H2XMMJ140125.3+024620 ^a	14 01 25.3 +02 46 20	14 01 25.2 +02 46 21	9.2	1.2	0.9970	1.29	20.99	AGN2	0.4332	42.91
		14 01 25.3 +02 46 19		1.6	0.9493	–	23.94	–	–	–
H2XMMJ140117.5+024349 ^a	14 01 17.5 +02 43 49	14 01 17.5 +02 43 51	10.2	2.1	0.9979	2.70	19.60	AGN1	0.3630	43.06
		14 01 17.5 +02 43 48		1.0	0.9866	–	23	–	–	–
H2XMMJ140115.0+024821	14 01 15.0 +02 48 21	14 01 15.2 +02 48 19	6.0	3.4		1.66	19.75	AGN1	1.5229	44.31
H2XMMJ140109.9+024339 ^a	14 01 09.9 +02 43 39	14 01 09.9 +02 43 39	9.7	0.2	1	1.53	20.75	AGN1	1.3550	44.15
		14 01 09.9 +02 43 37		2.4	0.9664	–	–	ETG	0.9356	–
H2XMMJ140109.0+025651	14 01 09.0 +02 56 51	14 01 08.8 +02 56 50	4.3	3.7		2.48	22.57	AGN1	1.8330	44.67
H2XMMJ140057.3+023942	14 00 57.3 +02 39 42	14 00 57.4 +02 39 43	13.5	1.6		3.64	19.50	ETG	0.2650	42.88
H2XMMJ140053.1+024150	14 00 53.1 +02 41 50	14 00 53.0 +02 41 51	11.4	1.3		2.07	23.61	–	–	–
H2XMMJ140053.1+030104 ^a	14 00 53.1 +03 01 04	14 00 53.1 +03 01 06	8.2	1.3	0.9985	5.02	20.18	AGN1	1.3045	44.63
		14 00 53.2 +03 01 10		5.9	0.6339	–	22.80	–	–	–
H2XMMJ140051.1+025906	14 00 51.1 +02 59 06	14 00 51.4 +02 59 05	6.4	4.1		2.14	18.99	AGN2	0.2564	42.61
H2XMMJ140049.1+025850	14 00 49.1 +02 58 50	14 00 49.0 +02 58 53	6.4	3.5		1.41	21.23	AGN1 ^b	1.8222	44.42
H2XMMJ140040.9+025353	14 00 40.9 +02 53 53	14 00 40.8 +02 53 53	5.0	1.4		1.75	24.19	–	–	–
H2XMMJ140038.7+024322	14 00 38.7 +02 43 22	14 00 38.6 +02 43 23	11.2	1.9		2.51	20.72	AGN1	0.6634	43.63
H2XMMJ140033.3+025810	14 00 33.3 +02 58 10	14 00 33.4 +02 58 13	8.5	3.4		2.05	22.87	AGN1	1.0260	44.00
H2XMMJ140033.0+025740	14 00 33.0 +02 57 40	14 00 33.3 +02 57 42	8.3	5.0		2.17	23.75	–	–	–
H2XMMJ140019.3+025638	14 00 19.3 +02 56 38	14 00 19.1 +02 56 40	10.9	4.0		2.33	22.52	AGN1	1.1115	44.13
H2XMMJ133807.5+242412	13 38 07.5 +24 24 12	13 38 07.5 +24 24 11	11.3	0.7		11.9	18.30	AGN1	0.6336	44.27
H2XMMJ133712.7+243251	13 37 12.7 +24 32 51	13 37 12.8 +24 32 54	9.9	3.6		3.89	19.60	–	–	–
H2XMMJ133643.1+242646	13 36 43.1 +24 26 46	–	8.8	–		3.46	$\gtrsim 23.0$	–	–	–
H2XMMJ133630.2+242625	13 36 30.2 +24 26 25	13 36 30.0 +24 26 22	11.4	4.4		2.97	18.60	ELG	0.2551	42.75
H2XMMJ133702.2+242434	13 37 02.2 +24 24 34	13 37 02.2 +24 24 36	3.9	1.7		1.56	21.15	–	–	–
H2XMMJ133730.6+242306	13 37 30.6 +24 23 06	13 37 30.8 +24 23 05	2.8	3.5		3.19	20.50	AGN1	1.2798	44.42
H2XMMJ133717.9+242148 ^a	13 37 17.9 +24 21 48	13 37 17.9 +24 21 49	1.5	1.5	0.9905	1.72	22.07	AGN2	0.3431	42.81
		13 37 18.0 +24 21 44		4.5	0.8867	–	22.58	–	–	–
H2XMMJ133649.4+242004	13 36 49.4 +24 20 04	13 36 49.3 +24 20 00	7.2	3.3		3.86	20.03	–	–	–
H2XMMJ133714.0+241960	13 37 14.0 +24 19 60	13 37 14.1 +24 20 01	3.2	1.7		1.61	21.16	AGN1	1.5521	44.32
H2XMMJ133637.4+241935	13 36 37.4 +24 19 35	–	9.9	–		2.85	$\gtrsim 24.20$	–	–	–
H2XMMJ133749.2+241942	13 37 49.2 +24 19 42	13 37 49.5 +24 19 42	7.8	4.1		1.68	23.05	–	–	–
H2XMMJ133724.3+241922	13 37 24.3 +24 19 22	13 37 24.5 +24 19 23	3.9	2.8		1.48	23.29	–	–	–
H2XMMJ133659.3+241916 ^a	13 36 59.3 +24 19 16	13 36 59.4 +24 19 15	5.7	1.3	0.9953	2.30	21.75	ELG	0.5008	43.31
		13 36 59.0 +24 19 11		5.6	0.9572	–	20.7	–	–	–

Table 1. The HELLAS2XMM second source sample, continue

Id	X-ray Position (J2000)	Optical Position (J2000)	Offaxis (arcmin)	Δ (arcsec)	Prob	F(2-10 keV) (10^{-14} cgs)	R	Class.	z	$\log L_{2-10\text{keV}}$ (erg/s)
H2XMMJ125605.6+220719	12 56 05.6 +22 07 19	12 56 05.7 +22 07 19	13.1	1.8		4.74	20.07	AGN1	1.1450	44.47
H2XMMJ125625.6+220717	12 56 25.6 +22 07 17	12 56 25.7 +22 07 20	9.1	3.3		2.17	20.55	AGN1	1.7310	44.56
H2XMMJ125719.2+220030	12 57 19.2 +22 00 30	12 57 19.4 +22 00 32	5.2	3.4		1.19	21.07	AGN1	1.5060	44.15
H2XMMJ125704.3+220037	12 57 04.3 +22 00 37	12 57 04.1 +22 00 40	2.1	4.3		0.83	23.44	–	–	–
H2XMMJ125647.4+215946	12 56 47.4 +21 59 46	12 56 47.2 +21 59 47	3.2	2.6		1.67	22.18	–	–	–
H2XMMJ125602.8+215952	12 56 02.8 +21 59 52	12 56 02.7 +21 59 52	12.8	1.4		11.1	19.10	–	–	–
H2XMMJ125750.6+215936	12 57 50.6 +21 59 36	12 57 50.5 +21 59 34	12.5	2.2		2.55	18.90	AGN1	0.6150	43.56
H2XMMJ125632.8+215936 ^a	12 56 32.8 +21 59 36	12 56 32.8 +21 59 37	6.2	1.1	0.9989	3.07	20.10	AGN1 ^c	0.5160	43.47
		12 56 33.2 +21 59 37		5.8	0.9341	–	21.26	ELG	0.2790	–
H2XMMJ125709.0+215800	12 57 09.0 +21 58 00	12 57 08.9 +21 57 57	4.8	3.1		0.67	20.79	AGN1	0.9112	43.39
H2XMMJ125629.4+215704	12 56 29.4 +21 57 04	12 56 29.3 +21 57 06	8.1	2.3		1.27	22.41	AGN1 ^d	0.6346	43.30
H2XMMJ125732.6+215708	12 57 32.6 +21 57 08	12 57 32.7 +21 57 08	9.5	0.9		1.39	19.40	–	–	–
H2XMMJ125638.9+215625	12 56 38.9 +21 56 25	12 56 38.9 +21 56 26	7.0	1.0		1.01	22.64	ELG	0.4703	42.89
H2XMMJ125712.2+215523	12 57 12.2 +21 55 23	12 57 12.1 +21 55 22	7.4	1.6		1.14	20.78	AGN1	0.8000	43.49
H2XMMJ125637.3+215439	12 56 37.3 +21 54 39	12 56 37.0 +21 54 36	8.7	5.2		1.08	23.71	–	–	–
H2XMMJ125650.6+215458 ^a	12 56 50.6 +21 54 58	12 56 50.6 +21 54 59	7.2	0.7	0.9996	2.65	20.00	AGN1	0.6450	43.63
		12 56 50.9 +21 54 57		4.7	0.7478	–	22.81	–	–	–
H2XMMJ125706.3+215506 ^a	12 57 06.3 +21 55 06	12 57 06.2 +21 55 06	7.2	1.4	0.9737	0.99	22.85	AGN1	1.8750	44.30
		12 57 06.1 +21 55 04		3.5	0.9292	–	22.77	–	–	–
H2XMMJ125715.9+215432	12 57 15.9 +21 54 32	12 57 15.7 +21 54 31	8.5	2.6		1.82	19.32	AGN1	0.4011	42.99
H2XMMJ125712.2+215358	12 57 12.2 +21 53 58	12 57 12.3 +21 53 59	8.7	1.8		1.66	20.71	ELG	0.6854	43.49
H2XMMJ125640.3+215351	12 56 40.3 +21 53 51	12 56 40.4 +21 53 51	9.0	1.5		1.17	22.53	–	–	–
H2XMMJ125628.1+215405	12 56 28.1 +21 54 05	12 56 27.9 +21 54 06	10.4	2.6		5.58	19.69	AGN1	1.8670	45.04
H2XMMJ125710.6+215353	12 57 10.6 +21 53 53	12 57 10.2 +21 53 53	8.6	5.7		2.06	19.92	AGN1	0.7977	43.74
H2XMMJ125650.3+215329	12 56 50.3 +21 53 29	12 56 50.5 +21 53 30	8.6	3.3		1.25	18.69	ETG ^e	0.3991	42.82
H2XMMJ125659.0+215347 ^b	12 56 59.0 +21 53 47	12 56 58.8 +21 53 46	8.2	3.5		6.06	17.42	AGN2	0.1871	42.77
H2XMMJ125654.1+215318	12 56 54.1 +21 53 18	12 56 54.1 +21 53 17	8.7	1.0		2.44	20.76	AGN2	0.9093	43.95
H2XMMJ125653.7+215125 ^a	12 56 53.7 +21 51 25	12 56 53.6 +21 51 26	10.6	2.1	0.9936	5.17	20.47	AGN1 ^f	0.8940	44.26
		12 56 53.4 +21 51 24		4.7	0.8972	–	22.34	AGN2	0.9127	–
H2XMMJ125633.1+215147 ^a	12 56 33.1 +21 51 47	12 56 32.9 +21 51 52	11.6	4.9	0.9882	2.95	19.60	AGN1 ^c	0.8950	44.01
		12 56 33.0 +21 51 49		2.5	0.9856	–	21.36	ETG	0.7533	–
H2XMMJ110522.5+381103	11 05 22.5 +38 11 03	11 05 22.6 +38 11 05	11.8	2.1		2.19	19.96	AGN1	1.2585	44.23
H2XMMJ110522.0+381401	11 05 22.0 +38 14 01	11 05 22.0 +38 14 02	12.1	1.1		5.86	11.30	AGN2	0.0276	41.05
H2XMMJ110517.9+381051	11 05 17.9 +38 10 51	11 05 17.8 +38 10 51	10.9	1.7		2.24	22.17	–	–	–
H2XMMJ110512.3+382129	11 05 12.3 +38 21 29	11 05 12.8 +38 21 29	14.4	5.8		4.28	19.70	–	–	–
H2XMMJ110509.7+381253	11 05 09.7 +38 12 53	11 05 09.6 +38 12 55	9.5	2.7		1.39	23.41	–	–	–
H2XMMJ110449.2+381810	11 04 49.2 +38 18 10	11 04 49.2 +38 18 11	9.1	1.7		2.06	18.30	AGN1	1.9451	44.65
H2XMMJ110447.6+380407	11 04 47.6 +38 04 07	11 04 47.6 +38 04 07	8.3	0.6		1.59	21.30	AGN1	2.2670	44.69
H2XMMJ110444.2+381449	11 04 44.2 +38 14 49	11 04 43.9 +38 14 48	5.9	4.3		3.29	7.60	*	0.0000	40.00
H2XMMJ110438.2+382500	11 04 38.2 +38 25 00	11 04 38.1 +38 25 01	14.6	2.0		1.63	22.45	–	–	–
H2XMMJ110437.8+382304	11 04 37.8 +38 23 04	11 04 37.6 +38 23 02	12.6	2.1		1.57	22.06	–	–	–
H2XMMJ110435.2+382139	11 04 35.2 +38 21 39	–	11.2	–		1.26	≥ 23.30	–	–	–
H2XMMJ110431.5+380305	11 04 31.5 +38 03 05	–	7.9	–		1.26	≥ 23.50	–	–	–
H2XMMJ110424.9+380024	11 04 24.9 +38 00 24	–	10.4	–		1.54	≥ 23.50	–	–	–

Cocchia et al.: HELLAS2XMM optical identifications

Table 1. The HELLAS2XMM second source sample, continue

Id	X-ray Position (J2000)	Optical Position (J2000)	Offaxis (arcmin)	Δ (arcsec)	Prob	F(2-10 keV) (10^{-14} cgs)	R	Class.	z	$\log L_{2-10keV}$ (erg/s)
H2XMMJ110420.8+380443	11 04 20.8 +38 04 43	11 04 20.9 +38 04 37	6.0	6.1		1.28	23.34	–	–	–
H2XMMJ110418.2+382047	11 04 18.2 +38 20 47	11 04 18.3 +38 20 47	10.1	0.6		2.66	22.10	AGN1	2.0487	44.82
H2XMMJ110416.2+380241	11 04 16.2 +38 02 41	11 04 16.0 +38 02 36	8.2	5.6		2.08	20.52	–	–	–
H2XMMJ110414.7+380714	11 04 14.7 +38 07 14	11 04 14.8 +38 07 15	3.8	0.9		5.70	22.75	–	–	–
H2XMMJ110413.2+382203	11 04 13.2 +38 22 03	11 04 13.3 +38 22 07	11.4	4.6		1.15	21.00	–	–	–
H2XMMJ110402.8+375950	11 04 02.8 +37 59 50	11 04 03.0 +37 59 50	11.6	2.2		3.75	20.52	AGN1	0.2864	42.97
H2XMMJ110345.8+380546	11 03 45.8 +38 05 46	11 03 46.3 +38 05 49	8.8	6.0		2.46	22.20	–	–	–
H2XMMJ110343.6+381349	11 03 43.6 +38 13 49	11 03 43.6 +38 13 49	8.2	0.5		2.80	22.85	–	–	–
H2XMMJ110339.9+380014	11 03 39.9 +38 00 14	11 03 40.0 +38 00 11	13.5	3.5		3.42	19.50	AGN2	0.3078	43.00
H2XMMJ110330.2+381607	11 03 30.2 +38 16 07	11 03 30.1 +38 16 06	11.6	1.7		1.35	22.75	–	–	–
H2XMMJ110325.8+381212	11 03 25.8 +38 12 12	11 03 25.9 +38 12 11	11.3	1.4		5.68	14.40	AGN2	0.0696	41.82
H2XMMJ110322.6+380945	11 03 22.6 +38 09 45	11 03 22.8 +38 09 45	11.8	1.6		2.46	21.85	–	–	–
H2XMMJ110318.6+381545	11 03 18.6 +38 15 45	11 03 18.4 +38 15 44	13.5	2.6		6.87	18.98	AGN1	0.3140	43.32
H2XMMJ110317.1+381336	11 03 17.1 +38 13 36	11 03 17.4 +38 13 38	13.2	4.0		3.66	19.51	AGN1	1.2506	44.45
H2XMMJ005019.4–515532	00 50 19.4 –51 55 32	00 50 19.5 –51 55 30	14.5	1.6		2.50	21.60	–	–	–
H2XMMJ005026.3–515929	00 50 26.3 –51 59 29	00 50 26.3 –51 59 30	11.3	1.3		1.89	22.30	–	–	–
H2XMMJ005009.4–515933	00 50 09.4 –51 59 33	00 50 09.7 –51 59 32	10.2	2.8		4.38	20.05	–	–	–
H2XMMJ005030.6–520011	00 50 30.6 –52 00 11	00 50 30.8 –52 00 10	11.0	1.9		13.5	18.78	AGN1	0.4630	44.00
H2XMMJ005030.7–520046 ^g	00 50 30.7 –52 00 46	00 50 30.9 –52 00 48	10.5	2.4		2.62	24.08	AGN2	1.3553 ^h	44.39
H2XMMJ005043.4–520116	00 50 43.4 –52 01 16	00 50 43.7 –52 01 17	11.4	3.1		2.02	21.18	–	–	–
H2XMMJ005126.5–520220	00 51 26.5 –52 02 20	00 51 26.2 –52 02 21	16.3	3.0		4.02	20.20	–	–	–
H2XMMJ005008.4–520350	00 50 08.4 –52 03 50	–	6.1	–		0.96	$\gtrsim 22.50$	–	–	–
H2XMMJ004953.1–520525	00 49 53.1 –52 05 25	00 49 52.9 –52 05 24	3.9	1.9		0.95	21.65	–	–	–
H2XMMJ005031.6–520630 ^g	00 50 31.6 –52 06 30	00 50 31.5 –52 06 34	6.9	4.1		1.63	24.04	–	$> 1.30^g$	–
H2XMMJ005017.1–520715	00 50 17.1 –52 07 15	00 50 17.4 –52 07 18	4.6	4.5		0.71	23.40	–	–	–
H2XMMJ005044.7–520735	00 50 44.7 –52 07 35	00 50 44.7 –52 07 36	8.5	0.9		1.02	19.84	–	–	–
H2XMMJ005012.3–520834	00 50 12.3 –52 08 34	00 50 12.3 –52 08 36	3.4	2.2		0.61	22.28	–	–	–
H2XMMJ004959.0–521112	00 49 59.0 –52 11 12	00 49 59.0 –52 11 10	2.3	1.4		1.05	21.26	–	–	–
H2XMMJ004955.7–521231	00 49 55.7 –52 12 31	–	3.3	–		0.76	$\gtrsim 22.50$	–	–	–
H2XMMJ004947.6–521249	00 49 47.6 –52 12 49	00 49 47.8 –52 12 48	3.5	1.9		2.66	21.04	AGN1	1.1046	44.19
H2XMMJ004936.7–521306 ^a	00 49 36.7 –52 13 06	00 49 36.7 –52 13 07	4.3	0.3	0.9999	0.96	20.31	AGN1	0.9290	43.57
		00 49 37.2 –52 13 07		4.6	0.9421	–	21.56	–	–	–
H2XMMJ004950.9–521410	00 49 50.9 –52 14 10	00 49 51.1 –52 14 13	4.8	2.9		2.22	22.30	–	–	–
H2XMMJ004959.4–521412	00 49 59.4 –52 14 12	00 49 59.2 –52 14 11	5.1	1.9		1.40	21.70	–	–	–
H2XMMJ004935.2–521458	00 49 35.2 –52 14 58	00 49 35.9 –52 14 56	6.1	6.7		1.11	20.42	–	–	–
H2XMMJ005007.4–521508 ^a	00 50 07.4 –52 15 08	00 50 07.4 –52 15 08	6.3	0.6	0.9998	1.41	19.43	AGN1 ^b	2.4220	44.71
		00 50 07.7 –52 15 06		3.3	0.9563	–	22.68	–	–	–
H2XMMJ005032.1–521543	00 50 32.1 –52 15 43	00 50 32.2 –52 15 43	9.0	0.5		6.41	19.77	AGN1	1.2224	44.67

Classification: AGN1; AGN2; ELG=Emission-Line Galaxy; ETG=Early-Type Galaxy; *=Star; ^a Two possible counterparts within 6''; ^b Broad absorption line QSO; ^c Two nearby objects, a type 1 AGN and an emission-line galaxy; ^d Tentative classification: low S/N spectrum; ^e Extended, emission from a group or cluster of galaxies; ^f Two nearby objects, a type 1 AGN and a type 2 AGN; ^g Aperture photometry at the position of a bright K source and photometric z (Mignoli et al. 2004); ^h Near-infrared spectroscopy (Maiolino et al. 2006).

Table 3. The HELLAS2XMM [OIII] sample

Observation Id	z	Class.	$\log L_{2-10\text{keV}}$ (erg/s)	$\text{LogF}([\text{OIII}])$ (cgs)	$\text{LogL}([\text{OIII}])$ (erg/s)
H2XMMJ054034.2-283108	0.3794	AGN2	43.44	-15.44 ^a	41.12 ^a
H2XMMJ054024.7-284616	0.4844	AGN2	43.02	-16.35	40.43
H2XMMJ053959.0-283753	0.8420	AGN1	43.93	-14.96	42.31
H2XMMJ053929.5-284860	0.3171	AGN1	43.55	-15.32	41.08
H2XMMJ053910.7-283528	0.7700	AGN1	43.95	-14.64	42.55
H2XMMJ053850.9-283757	0.7630	AGN1	44.2	-14.82	42.36
H2XMMJ031416.4-764536	0.2456	AGN1	42.74	-15.3	40.87
H2XMMJ031200.4-770026	0.8410	AGN2	43.79	-16.59	40.68
H2XMMJ031136.0-765556	0.7090	ELG	43.49	-16.46	40.66
H2XMMJ031112.8-764706	0.7530	AGN1	43.72	-16.27	40.9
H2XMMJ031050.0-763904	0.3812	AGN1	44.12	-15.46 ^a	41.1 ^a
H2XMMJ031037.4-764713	0.6410	ELG	43.43	-15.57	41.46
H2XMMJ030951.2-765825	0.2060	ELG	42.66	-15.87	40.14
H2XMMJ030912.1-765826	0.2651	AGN2	43.3	-15.03	41.2
H2XMMJ235933.4-250758	0.7380	AGN1	43.88	-15.63	41.52
H2XMMJ000102.4-245847	0.4331	AGN1	43.85	-16.22	40.46
H2XMMJ000100.2-250459	0.8504	AGN1	44.66	-15.04	42.24
H2XMMJ000036.6-250105	0.5917	AGN2	43.64	-15.85	41.11
H2XMMJ000031.7-245459	0.2839	AGN1	43.35	-14.83	41.47
H2XMMJ000027.7-250441	0.3362	AGN1	43.43	-14.78	41.67
H2XMMJ000026.0-250648	0.4331	AGN1	43.03	-15.8	40.88
H2XMMJ003418.5-120809	0.2327	AGN2	43.04	-15.24	40.88
H2XMMJ204446.4-103839	0.6941	AGN2	43.84	-14.77	42.33
H2XMMJ204349.2-103746	0.5556	AGN1	43.82	-14.88	42.02
H2XMMJ140139.6+025722	0.2490	AGN1	42.64	-15.11	41.07
H2XMMJ140130.8+024532	0.7456	ELG	43.97	-15.74	41.42
H2XMMJ140125.3+024620	0.4332	AGN2	42.91	-14.36	42.32
H2XMMJ140117.5+024349	0.3630	AGN1	43.06	-15.2 ^a	41.32 ^a
H2XMMJ140051.1+025906	0.2564	AGN2	42.61	-14.53	41.67
H2XMMJ140038.7+024322	0.6634	AGN1	43.63	-15.78	41.28
H2XMMJ133630.2+242625	0.2551	ELG	42.75	-15.15	41.05
H2XMMJ133717.9+242148	0.3431	AGN2	42.81	-16.12	40.34
H2XMMJ133659.3+241916	0.5008	ELG	43.31	-15.89	40.92
H2XMMJ125632.8+215936	0.5160	AGN1	43.47	-15.78 ^b	41.06 ^b
H2XMMJ125709.0+215800	0.9112	AGN1	43.39	-16.04	41.3
H2XMMJ125629.4+215704	0.6346	AGN1	43.30	-16.51	40.51
H2XMMJ125638.9+215625	0.4703	ELG	42.89	-16.68	40.07
H2XMMJ125712.2+215523	0.8000	AGN1	43.49	-16.39	40.84
H2XMMJ125715.9+215432	0.4011	AGN1	42.99	-15.64	40.97
H2XMMJ125712.2+215358	0.6854	ELG	43.49	-16.59	40.5
H2XMMJ125710.6+215353	0.7977	AGN1	43.74	-15.88	41.34
H2XMMJ125659.0+215347	0.1871	AGN2	42.77	-14.56	41.37
H2XMMJ125654.1+215318	0.9093	AGN2	43.95	-15.59	41.75
H2XMMJ110522.0+381401	0.0276	ELG	41.05	-14.36	39.92
H2XMMJ110402.8+375950	0.2864	AGN1	42.97	-15.21	41.09
H2XMMJ110339.9+380014	0.3078	AGN2	43.00	-15.02	41.35
H2XMMJ110325.8+381212	0.0696	AGN2	41.82	-14.68	40.36
H2XMMJ110318.6+381545	0.3140	AGN1	43.32	-14.81	41.58
H2XMMJ005030.6-520011	0.4630	AGN1	44.00	-14.71	42.02
H2XMMJ053925.8-284456	0.0750	ETG	41.82	< -16.70	< 38.41
H2XMMJ031239.3-765133	0.1590	ETG	42.24	< -16.80	< 38.98
H2XMMJ031231.2-764324	0.0520	ETG ^c	41.08	< -16.26	< 38.54
H2XMMJ031124.8-770139	0.3199	ETG	42.93	< -16.42	< 39.98
H2XMMJ030952.2-764927	0.2049	ETG	42.22	< -16.74	< 39.26
H2XMMJ000030.1-251214	0.1543	ETG ^c	42.07	< -16.00	< 39.75
H2XMMJ204420.5-104904	0.3240	ETG	43.16	< -16.67	< 39.75
H2XMMJ140144.9+025332	0.2506	ETG	42.97	< -16.03	< 40.16
H2XMMJ140057.3+023942	0.2650	ETG	43.02	< -16.31	< 39.92
H2XMMJ125650.3+215329	0.3991	ETG ^c	42.82	< -17.18	< 39.43

Table 4. IAU names for the HELLAS2XMM source sample

IAU name	Id	IAU name	Id	IAU name	Id
H2XMMJ053925.8–284456	05370024 ^a	H2XMMJ133714.0+241960	13390131	H2XMMJ005030.6–520011	16274066
H2XMMJ054034.2–283108	05370008 ^a	H2XMMJ133637.4+241935	13390133	H2XMMJ005030.7–520046	16274069
H2XMMJ054024.7–284616	05370135 ^a	H2XMMJ133749.2+241942	13390134	H2XMMJ005043.4–520116	16274078
H2XMMJ053959.0–283753	05370007 ^a	H2XMMJ133724.3+241922	13390137	H2XMMJ005126.5–520220	16274097
H2XMMJ053929.5–284860	05370003 ^a	H2XMMJ133659.3+241916	13390140	H2XMMJ005008.4–520350	16274117
H2XMMJ053910.7–283528	05370009 ^a	H2XMMJ125605.6+220719	15300065	H2XMMJ004953.1–520525	16274158
H2XMMJ053850.9–283757	05370020 ^a	H2XMMJ125625.6+220717	15300067	H2XMMJ005031.6–520630	16274181
H2XMMJ031239.3–765133	03120018 ^a	H2XMMJ125719.2+220030	15300142	H2XMMJ005017.1–520715	16274197
H2XMMJ031231.2–764324	03120008 ^a	H2XMMJ125704.3+220037	15300143	H2XMMJ005044.7–520735	16274212
H2XMMJ031124.8–770139	03120017 ^a	H2XMMJ125647.4+215946	15300148	H2XMMJ005012.3–520834	16274235
H2XMMJ030952.2–764927	03120501 ^a	H2XMMJ125602.8+215952	15300151	H2XMMJ004959.0–521112	16274292
H2XMMJ031416.4–764536	03120010 ^a	H2XMMJ125750.6+215936	15300152	H2XMMJ004955.7–521231	16274307
H2XMMJ031200.4–770026	03120016 ^a	H2XMMJ125632.8+215936	15300153	H2XMMJ004947.6–521249	16274314
H2XMMJ031136.0–765556	03120181 ^a	H2XMMJ125709.0+215800	15300176	H2XMMJ004936.7–521306	16274320
H2XMMJ031112.8–764706	03120011 ^a	H2XMMJ125629.4+215704	15300186	H2XMMJ004950.9–521410	16274339
H2XMMJ031050.0–763904	03120007 ^a	H2XMMJ125732.6+215708	15300189	H2XMMJ004959.4–521412	16274340
H2XMMJ031037.4–764713	03120028 ^a	H2XMMJ125638.9+215625	15300193	H2XMMJ004935.2–521458	16274349
H2XMMJ030951.2–765825	03120014 ^a	H2XMMJ125712.2+215523	15300203	H2XMMJ005007.4–521508	16274351
H2XMMJ030912.1–765826	03120034 ^a	H2XMMJ125637.3+215439	15300207	H2XMMJ005032.1–521543	16274363
H2XMMJ000030.1–251214	26900013 ^a	H2XMMJ125650.6+215458	15300208		
H2XMMJ235933.4–250758	26900028 ^a	H2XMMJ125706.3+215506	15300209		
H2XMMJ000102.4–245847	26900003 ^a	H2XMMJ125715.9+215432	15300216		
H2XMMJ000100.2–250459	26900002 ^a	H2XMMJ125712.2+215358	15300219		
H2XMMJ000036.6–250105	26900022 ^a	H2XMMJ125640.3+215351	15300222		
H2XMMJ000031.7–245459	26900004 ^a	H2XMMJ125628.1+215405	15300225		
H2XMMJ000027.7–250441	26900001 ^a	H2XMMJ125710.6+215353	15300226		
H2XMMJ000026.0–250648	26900012 ^a	H2XMMJ125650.3+215329	15300230		
H2XMMJ003418.5–120809	15800012 ^a	H2XMMJ125659.0+215347	15300231		
H2XMMJ204420.5–104904	50900061 ^a	H2XMMJ125654.1+215318	15300236		
H2XMMJ204446.4–103839	50900036 ^a	H2XMMJ125653.7+215125	15300240		
H2XMMJ204349.2–103746	50900031 ^a	H2XMMJ125633.1+215147	15300253		
H2XMMJ140144.9+025332	18350140	H2XMMJ110522.5+381103	42100102		
H2XMMJ140144.8+024845	18350227	H2XMMJ110522.0+381401	42100058		
H2XMMJ140139.6+025722	18350069	H2XMMJ110517.9+381051	42100106		
H2XMMJ140137.1+024604	18350258	H2XMMJ110512.3+382129	42100269		
H2XMMJ140132.1+025222	18350155	H2XMMJ110509.7+381253	42100073		
H2XMMJ140130.8+024532	18350262	H2XMMJ110449.2+381810	42100302		
H2XMMJ140127.7+025607	18350095	H2XMMJ110447.6+380407	42100197		
H2XMMJ140125.3+024620	18350256	H2XMMJ110444.2+381449	42100039		
H2XMMJ140117.5+024349	18350279	H2XMMJ110438.2+382500	42100243		
H2XMMJ140115.0+024821	18350240	H2XMMJ110437.8+382304	42100258		
H2XMMJ140109.9+024339	18350281	H2XMMJ110435.2+382139	42100266		
H2XMMJ140109.0+025651	18350084	H2XMMJ110431.5+380305	42100207		
H2XMMJ140057.3+023942	18350033	H2XMMJ110424.9+380024	42100229		
H2XMMJ140053.1+024150	18350232	H2XMMJ110420.8+380443	42100189		
H2XMMJ140053.1+030104	18350034	H2XMMJ110418.2+382047	42100272		
H2XMMJ140051.1+025906	18350048	H2XMMJ110416.2+380241	42100212		
H2XMMJ140049.1+025850	18350052	H2XMMJ110414.7+380714	42100148		
H2XMMJ140040.9+025353	18350135	H2XMMJ110413.2+382203	42100264		
H2XMMJ140038.7+024322	18350283	H2XMMJ110402.8+375950	42100237		
H2XMMJ140033.3+025810	18350057	H2XMMJ110345.8+380546	42100170		
H2XMMJ140033.0+025740	18350061	H2XMMJ110343.6+381349	42100055		
H2XMMJ140019.3+025638	18350080	H2XMMJ110339.9+380014	42100231		
H2XMMJ133807.5+242412	13390094	H2XMMJ110330.2+381607	42100011		
H2XMMJ133712.7+243251	13390015	H2XMMJ110325.8+381212	42100088		
H2XMMJ133643.1+242646	13390060	H2XMMJ110322.6+380945	42100116		
H2XMMJ133630.2+242625	13390064	H2XMMJ110318.6+381545	42100025		
H2XMMJ133702.2+242434	13390085	H2XMMJ110317.1+381336	42100066		
H2XMMJ133730.6+242306	13390103	H2XMMJ005019.4–515532	16274019		
H2XMMJ133717.9+242148	13390112	H2XMMJ005026.3–515929	16274055		